Modeling and Advanced Control of Dual-Active-Bridge DC–DC Converters: A Review

Shuai Shao, *Member, IEEE*, Linglin Chen, Zhenyu Shan, *Member, IEEE*, Fei Gao, *Member, IEEE*, Hui Chen, Deshang Sha, *Senior Member, IEEE*, and Tomislav Dragičević, *Senior Member, IEEE*

***Abstract*—This article classifies, describes, and critically compares different modeling techniques and control methods for dual-active-bridge (DAB) dc–dc converters and provides explicit guidance about the DAB controller design to practicing engineers and researchers. First, available modeling methods for DAB including reduced-order model, generalized average model, and discrete-time model are classified and quantitatively compared using simulation results. Based on this comparison, recommendations for suitable DAB modeling method are given. Then, we comprehensively review the available control methods including feedback-only control, linearization control, feedforward plus feedback, disturbance-observer-based control, feedforward current control, model predictive current control, sliding mode control, and moving discretized control set model predictive control. Frequency responses of the closed-loop control-to-output and output impedance are selected as the metrics of the ability in voltage tracking and the load disturbance rejection performance. The frequency response plots of the closed-loop control-to-output transfer function and output impedance of each control method are theoretically derived or swept using simulation software PLECS and MATLAB. Based on these plots, remarks on each control method are drawn. Some practical control issues for DAB including dead-time effect, phase drift, and dc magnetic flux bias are also reviewed. This article is accompanied by PLECS simulation files of the reviewed control methods.**

Manuscript received January 21, 2021; revised May 14, 2021 and July 22, 2021; accepted August 19, 2021. Date of publication August 30, 2021; date of current version October 15, 2021. This work was supported in part by the National Key Research and Development Program of China under Grant 2018YFB0904100 and in part by the National Natural Science Foundation of China under Grant 52007168. Recommended for publication by Associate Editor Y. Siwakoti. *(Corresponding authors: Linglin Chen; Hui Chen.)*

Shuai Shao is with the College of Electrical Engineering and the Hangzhou Global Scientific and Technological Innovation Center, Zhejiang University, Hangzhou 310027, China (e-mail: shaos@zju.edu.cn).

Linglin Chen and Fei Gao are with the Department of Electrical Engineering, Shanghai Jiao Tong University, Shanghai 200240, China (e-mail: linglin.chen@nottingham.ac.uk; fei.gao@sjtu.edu.cn).

Zhenyu Shan is with the School of Automation Science and Electrical Engineering, Beihang University, Beijing 100083, China (e-mail: zhenyus@buaa.edu.cn).

Hui Chen is with the School of Information and Electrical Engineering, Zhejiang University City College, Hangzhou 310015, China (e-mail: chenh@zucc.edu.cn).

Deshang Sha is with the Advanced Power Conversion Center, School of Automation, Beijing Institute of Technology, Beijing 100081, China (e-mail: shadeshang@bit.edu.cn).

Tomislav Dragičević is with the Department of Electrical Engineering, Technical University of Denmark (DTU), 2800 Kongens Lyngby, Denmark (e-mail: tomdr@elektro.dtu.dk).

This article has supplementary material provided by the authors and color versions of one or more figures available at https://doi.org/10.1109/TPEL.2021.3108157.

Digital Object Identifier 10.1109/TPEL.2021.3108157

***Index Terms*—DC–DC, dual active bridge (DAB), reduced-order model, generalized average model, discrete-time model, feedback control, feedforward control, model predictive control.**

I. Introduction

DC MICROGRIDS have higher efficiency, better current carrying capacity, and faster dynamic response compared to the conventional ac systems [1]. They also provide more natural interface with many types of renewable energy systems (RESs) and energy storage systems (ESSs) and better compliance with consumer electronics [1]. These facts lead to increased applications of dc microgrid-type power architectures in remote households, data/telecom centers, RESs, electric vehicle charging stations, ships, aircraft, and others.

In dc microgrids, isolated bidirectional dc/dc (IBDC) power converters play an important role. IBDCs can serve as the interface of ESSs such as batteries and super capacitors to allow energy exchange between ESSs and the dc microgrid. They can also be stacked together to operate in the so-called solid-state transformer (SST) architecture, that can manage the power flow between dc microgrid and the upstream distribution network, as illustrated in Fig. 1.

Various IBDC topologies have been proposed, including bidirectional resonant converters, dual flyback, dual-Cuk, dual-push–pull, and dual active bridge (DAB) [4]. For the ESSs and microgrids applications, the DAB (see Fig. 2) originally proposed by de Doncker *et al.* [5], [6] is one of the most promising typologies for the following reasons [7].

1) Autoadjust bidirectional power flow, ideal for SSTs and ESSs in microgrids that often requires fast changes in the power flow direction.
2) Wide voltage conversion gain range, which is essential to interface ESSs such as batteries or supercapacitors, whose voltages can vary significantly under different states of charge.
3) Zero-voltage switching (ZVS) capability, able to achieve high efficiency with proper control.

Various applications employing DABs have been proposed. SSTs based on DABs in power grids have been introduced to interconnect different scale microgrids [8] or to connect different levels of dc grids [9], [10]. The power electronic traction transformer using DABs can reduce the weight, add additional functionalities, and improve the energy efficiency compared to the on-board line frequency transformer [11], [12]. DAB is also a promising solution for on-board battery chargers in plug-in

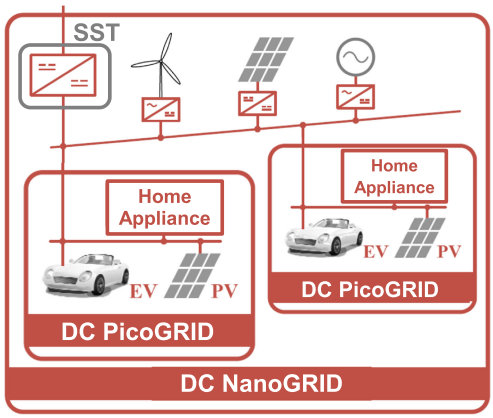

Fig. 1. Diagram of a hierarchical microgrid with SST as the energy router [2], [3].

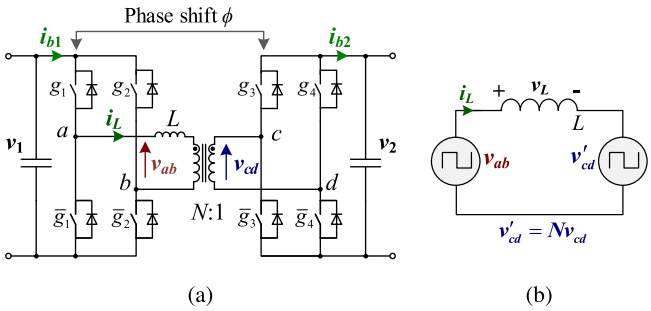

Fig. 2. Topology of (a) DAB converter and (b) its equivalent circuit.

electric vehicles, especially when the vehicle-to-grid function is required [13], [14]. With Gallium Nitride (GaN) devices, a 1-MHz 1.2-kW/400-V DAB prototype is reported to achieve 97.5% peak efficiency [15]. With 1700-V (silicon carbide) SiC devices, a 1500-V/200-kW DAB prototype is reported to achieve 99.6% peak efficiency [16], [17]. Other applications including ESS interface converters [18], airborne wind turbines [19], uninterrupted power supplies (UPS) [20], and power load emulators [21] have also been reported.

In all these applications, it is essential to model the DAB converter and design its controller with specified steady-state and dynamic performance. The aim of this article is to classify, describe, and critically compare different modeling techniques and control methods for DAB converters and provide explicit guidance about the DAB controller design to practicing engineers and researchers. Section II categorizes the available modeling techniques for the DAB including reduced-order model, generalized average model, and discrete-time model. These models are quantitatively compared based on simulation results. Section III comprehensively describes available control methods for DAB including feedback control, linearization control, feedforward plus feedback, disturbance-observer-based control (DOBC), feedforward current control (FFCC), model predictive current control, sliding mode control (SMC), and moving discretized control set model predictive control (MDCS-MPC). The closed-loop control-to-output $G_{ro}(s)$ and output impedance $Z_o(s)$ are selected as the metrics of the ability in voltage tracking

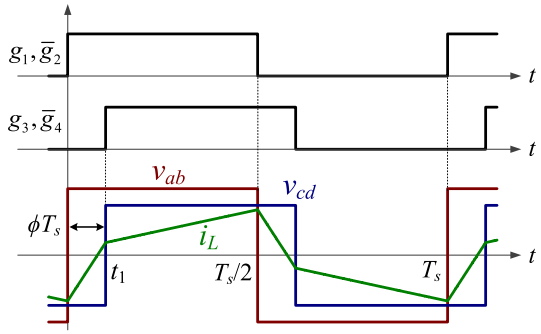

Fig. 3. Key waveforms of a DAB using SPS modulation.

and the load disturbance rejection performance. The frequency response plots of $G_{ro}(s)$ and $Z_o(s)$ of each control method are theoretically derived or swept using simulation software. Based on these plots, remarks on each control method are drawn. Section IV reviews some practical control issues including dead-time effect, phase drift, and dc magnetic flux bias. Finally, Section V concludes this article.

Compared to the existing reviews about modeling and control [4], [7], [22], [23], this article provides a more systematic overview of all known modeling and advanced control techniques for DAB. We are the first to quantitatively compare the available modeling methods and to recommend the most suitable models for the controller design. Moreover, we also comprehensively describe the implementation of several advanced control methods and systematically evaluate these methods in frequency domain. We believe that such an approach provides valuable contribution to the field as it gives practicing engineers and researchers a clear guidance on how to: choose an appropriate modeling technique, choose which control method is the most suitable for their application, and understand how to formally analyze the performance of the DAB converter in practice and implement its associated controller.

II. Modeling of a DAB

Modeling is the representation of a physical phenomenon by mathematical means [24]. DAB modeling is more challenging compared to modeling of conventional dc–dc converters as one of the state variables, the inductor current i_L, is purely ac with an average value 0, as shown in Fig. 3. This section summarizes modeling methods for a DAB converter, and compares the large- and small-signal models obtained from these methods using simulation results to give guidance for the DAB controller design. The modeling methods are introduced based on a DAB using the single-phase-shift (SPS) modulation (see Fig. 3), but these methods can be extended to a DAB using dual-phase-shift (DPS) or triple-phase-shift (TPS) modulation [7].

A. Reduced-Order Model

One way to model DAB is simply ignoring the dynamics of i_L, which is called reduced-order model [25]–[27]. The average values of input and output currents over one switching cycle (or half a cycle) are used to describe the characteristics of the

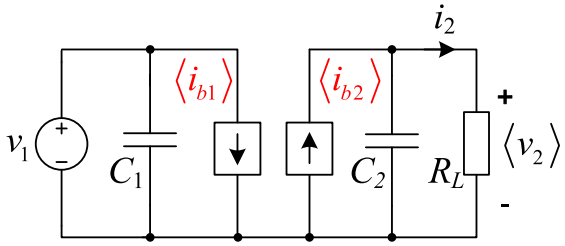

Fig. 4. Large-signal diagram of the DAB reduced-order model [25]–[27].

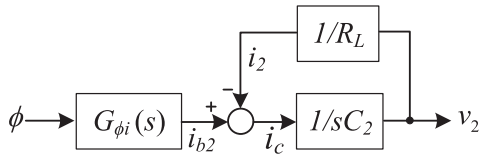

Fig. 5. Block diagram of the reduced-order model.

current. Then, a DAB is simplified to a first-order system, as shown in Fig. 4, where $\langle i_{b1} \rangle$ and $\langle i_{b2} \rangle$ are the switching cycle average of the currents i_{b1} and i_{b2} (see Fig. 2).

The output power P_o of a DAB modulated using the SPS can be expressed as [6]

$$P_o = \frac{N v_1 v_2 \phi (1 - 2|\phi|)}{f_s L} \tag{1}$$

where N, v_1, v_2, ϕ, and L are illustrated in Figs. 2 and 3, and f_s is the switching frequency of a DAB. Since $P_o = v_2 \langle i_{b2} \rangle$, $\langle i_{b2} \rangle$ can be calculated under the positive power flow

$$\langle i_{b2} \rangle = \frac{N v_1 \phi (1 - 2\phi)}{f_s L}. \tag{2}$$

Introducing perturbation at phase shift, $\phi = \Phi + \hat{\phi}$, $\langle i_{b2} \rangle = I_{b2} + \hat{i}_{b2}$, we obtain the transfer function from ϕ to i_{b2}

$$G_{\phi i}(s) = \frac{\hat{i}_{b2}}{\hat{\phi}} = \frac{d \langle i_{b2} \rangle}{dt} = \frac{N V_1 (1 - 4\Phi)}{f_s L} \tag{3}$$

where V_1, V_2, Φ, and I_{b2} are the quiescent values of $v_1, v_2, \phi,$ and i_{b2}. Φ and I_{b2} can be expressed as

$$\Phi = \begin{cases} \frac{1}{4} - \sqrt{\frac{1}{16} - \frac{f_s L I_2}{2 N V_1}} & I_2 \geq 0 \\ -\frac{1}{4} + \sqrt{\frac{1}{16} + \frac{f_s L I_2}{2 N V_1}} & I_2 < 0 \end{cases} \tag{4}$$

$$I_{b2} = I_2 = V_2 / R_L. \tag{5}$$

Based on Fig. 4 and (3), the control block diagram from ϕ to v_2 is shown in Fig. 5. The transfer function from ϕ to v_2 can be derived as

$$G_{v\phi}(s) = \frac{\hat{v}_2}{\hat{\phi}} = \frac{N V_1 (1 - 4\Phi)}{f_s L} \frac{R_L}{R_L C_2 s + 1}. \tag{6}$$

Based on the aforementioned analysis, the reduced-order model of DAB is a first-order system. For DAB modulated using the DPS and TPS, the circuit model can also be represented using Figs. 4 and 5. The difference between the models of these

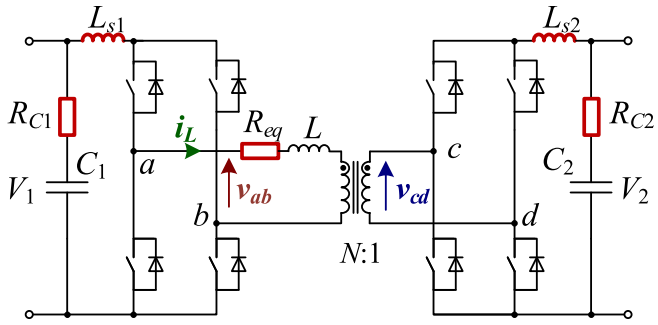

Fig. 6. DAB circuit considering the parasitic parameters.

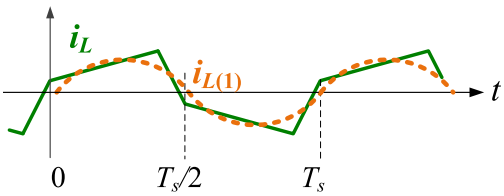

Fig. 7. Waveform of the inductor current i_L and its fundamental component $i_{L(1)}$.

methods is the gain $G_{\phi i}(s)$. It is more complex to compute this gain for DAB modulated using the DPS or TPS, compared to DAB with the SPS. The reduced-order model for DAB with the TPS is presented in [28]. Besides, it is possible to consider the parasitic parameters to slightly improve the reduced-order model as shown in Fig. 6, where the parasitic parameters ($R_{\text{eq}}, R_{c1}, R_{c2}, L_{s1},$ and L_{s2}) are indicated using red color [29]. The resultant model is more complex by considering these insignificant parasitics. Actually, we will show in Section II-D that the reduced-order model (see Fig. 5) is accurate enough for the controller design.

B. Generalized Average Model

To include the dynamics of i_L, a generalized averaging technique can be applied to model the DAB. This averaging method is based on the representation of a signal $x(\tau)$ on the interval $\tau \in [t - T, t]$ by the Fourier series [30]–[32]

$$x(\tau) = \sum_{-\infty}^{\infty} \langle x \rangle_k (t) e^{jk\omega_s \tau} \tag{7}$$

where $\omega_s = 2\pi f_s$, and the complex number $\langle x \rangle_k (t)$ is the kth coefficient.

The conventional state-space averaging is a special case of the generalized average modeling method, in which only the dc term ($k = 0$) is considered. In the case of a DAB, the inductor current i_L is purely ac and it is natural to include more terms, and in [31], fundamental component of i_L ($k = \pm 1$, Fig. 7) and dc term of the output voltage (v_2) are considered. The state-space equation and small-signal perturbation are employed to derive the small-signal model [31]

$$\begin{cases} d\mathbf{x}/dt = \mathbf{A}\mathbf{x} + \mathbf{B}\mathbf{U} \\ \mathbf{y} = \mathbf{C}\mathbf{x} \end{cases} \tag{8}$$

where $\mathbf{x} = [\hat{v}_{2(0)}\ \hat{i}_{LR(1)}\ \hat{i}_{LI(1)}]^T$ and $\mathbf{y} = [\hat{v}_{2(0)}]$. The subscripts "*R*" and "*I*" mean the real and imaginary parts of a complex number, respectively, whereas the subscripts 0 and 1 mean the dc component and fundamental frequency component, respectively. **A**, **B**, and **C** are expressed as

$$\mathbf{A} = \begin{bmatrix} -\dfrac{2}{R_L C_2} & -\dfrac{8N\sin(2\pi\Phi)}{\pi C_2} & \dfrac{-8N\cos(2\pi\Phi)}{\pi C_2} \\ \dfrac{4N\sin(2\pi\Phi)}{\pi L} & -\dfrac{2R_{eq}}{L} & 2\omega_s \\ \dfrac{4N\cos(2\pi\Phi)}{\pi L} & -2\omega_s & -\dfrac{2R_{eq}}{L} \end{bmatrix}$$

$$\mathbf{B} = \begin{bmatrix} \dfrac{8}{C_2}\left(I_{LI(1)}\sin(2\pi\Phi) - I_{LR(1)}\cos(2\pi\Phi)\right) \\ \dfrac{4V_{2(0)}}{L}\sin(2\pi\Phi) \\ -\dfrac{4V_{2(0)}}{L}\sin(2\pi\Phi) \end{bmatrix}$$

$$\mathbf{C} = \begin{bmatrix} 1\ 0\ 0 \end{bmatrix}^T$$

where $V_{2(0)}, I_{LI(1)},$ and $I_{LR(1)}$ are the quiescent values of the state variables $v_{2(0)}, i_{LI(1)},$ and $i_{LR(1)}$, respectively.

The transfer function from the phase shift ϕ to output voltage v_2 can be derived as follows:

$$G_{v\phi}(s) = \mathbf{C}(s\mathbf{I} - \mathbf{A})^{-1}\mathbf{B}. \tag{9}$$

The resultant model can reflect the dynamics of i_L.

C. Discrete-Time model

Same as the generalized average model, the discrete-time model can include high-frequency dynamics and is used for DAB modeling [33]–[37]. The discrete-time model views the state variables as only being changed at separate points of time. Consider a DAB modulating using the SPS, there are four switching states in a switching cycle as shown in Fig. 8(a) and the state-space equations can be obtained in each state as shown in Fig. 8(b). Then, the state at $t = (k+1)T$, $\mathbf{x[k+1]}$ can be expressed using $\mathbf{x[k]}$ as

$$\mathbf{x[k+1]} = \mathbf{Fx[k]} + \mathbf{GU[k]} \tag{10}$$

where $\mathbf{x} = [i_L, v_2]^T$, $U = [v_1]$, and the vectors **F** and **G** can be calculated based on the state-space equation and period of each state shown in Fig. 8, and were derived in [37]. The corresponding small-signal discrete-time model is obtained by introducing a phase perturbation $\hat{\phi}[k]$ around the steady-state time-varying vector $\mathbf{x[t]}$ as shown in Fig. 9 [35], [38]. Because the converter has two phase-shift intervals per switching period, a phase perturbation alters the state at two points t_{p1} and t_{p2}, and the net results of phase perturbation at these two points are $\hat{x}_{d1}$ and $\hat{x}_{d2}$, as shown in Fig. 9. The instantaneous state perturbations are propagated to the end of the switching period through χ_1 and χ_2, which are calculated in [35]. The small-signal model can be derived accordingly.

Using the discrete-time modeling method, very accurate models can be obtained for high-frequency or digitally controlled converters. This method can easily consider the ZVS transition,

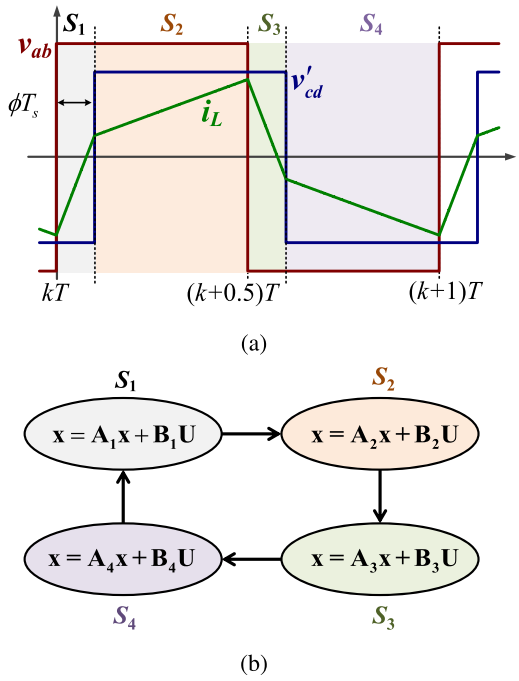

Fig. 8. Discrete-time modeling for a DAB. (a) States definition. (b) State-space equation in each state.

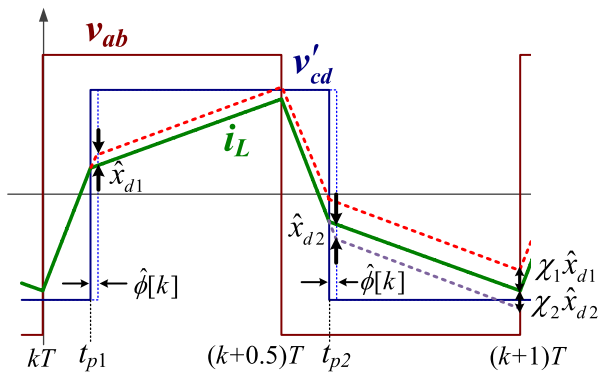

Fig. 9. Small-signal modeling based on the discrete-time model.

as well as the sampling, modulator effects, and delays in the digitally control loop. The drawback of the discrete-time model is the complex calculation due to the product of matrix exponentials. This is especially the case for a DAB since there are at least four states in each switching cycle [35]. To simplify the calculation, the matrix exponential can be simplified by its bilinear Taylor series, $\mathbf{e}^{\mathbf{A_i t_i}} \approx \mathbf{I} + \mathbf{A_i t_i}$ or through a modified bilinear expansion [33], [36], [37]. Still, the calculation of the discrete method is much more complex than that of the continuous ones, and software such as MATLAB are required to complete the calculation.

D. Comparison of Different DAB Modeling Methods

The four different DAB models, reduced-order model [25], [26], improved reduced-order model [29], generalized average model [31], and discrete-time model [35], [37], are compared

TABLE I
DAB CIRCUIT PARAMETERS USED FOR MODEL COMPARISON

		Nominal value[a]
N	Transformer turns ratio	2:1
f_s	Switching frequency	20kHz
L	Inductance	$L_0 = 70\mu$H
R_{eq}	Equivalent resistance	$R_{eq0} = 0.25\Omega$
C_2	DC Capacitor 2	$C_{20} = 1m$F
R	Load resistor	4Ω
T_d	Dead time	200ns

a: The nominal value is the value used in the DAB circuit. The circuit parameters used in the control can be different from this nominal value.

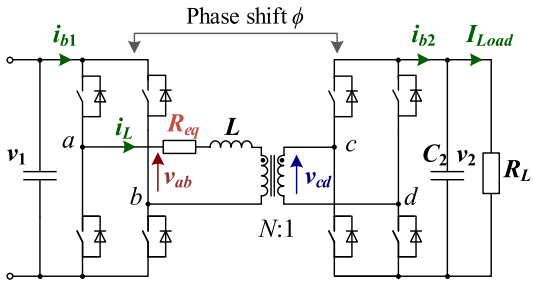

Fig. 10. DAB circuit for model comparison.

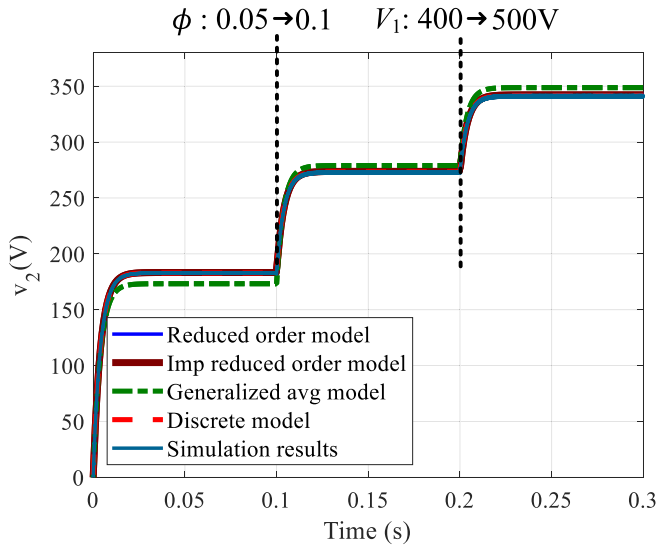

Fig. 11. Comparison of large-signal models.

with simulation results. The comparisons are based on a DAB with parameters listed in Table I, an equivalent resistor R_{eq} is included to represent the power losses caused by power devices and transformers as shown in Fig. 10. A dead time 200 ns is considered in the simulation.

Fig. 11 shows the comparison of the large-signal models with simulation results, in which at $t = 0.1$ s, the phase shift ratio ϕ steps from 0.05 to 0.1, and at $t = 0.2$ s, the input voltage V_1 steps from 400 to 500 V. All the four models predict v_2 step response pretty well, however, the generalized average model has some steady-state errors because the third and higher order components of i_L are ignored.

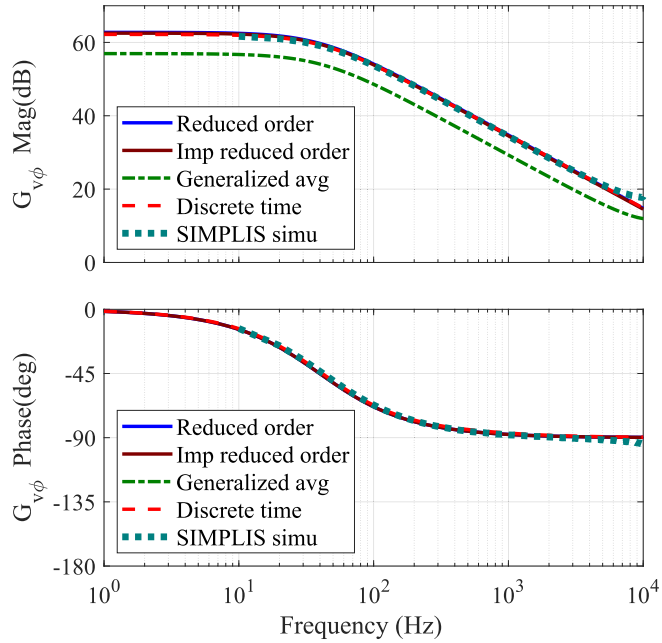

Fig. 12. Comparison of the bode plot of small-signal models $G_{v\phi}$ (from ϕ to v_2).

TABLE II
COMPARISON OF DAB MODELING METHODS

Modeling methods	**Model complexity**	**Large signal accuracy**	**small signal accuracy**
Reduced order [25]	Low	++++	++++
Imp reduced order [29]	Medium	++++	++++
Generalized average [31]	Medium	++	++
Discrete time [35], [37]	High	++++	++++

Note: **+ = Poor**; **++ = Average**; **+++ = Good**; **++++ = Excellent**

Fig. 12 shows the bode plot of small-signal models $G_{v\phi}(s)$ (open-loop transfer function from ϕ to v_2) obtained using different modeling methods. For comparison, the simulated small-signal response obtained through ac analysis in SIMetrix/SIMPLIS is also plotted. The operating conditions are $V_1 = 400V, \Phi = 0.1$, and other parameters are listed in Table I. Except for the generalized average model, all the other models correspond well to the simulated model both for the magnitude and phase. The generalized average model has a magnitude error because the third and higher order components of i_L are ignored.

Table II compares the performance of different modeling methods in terms of modeling accuracy and model complexity. The performance on the model accuracy is based on the results in Figs. 11 and 12, whereas the model complexity is based on the number of equations of each model. As shown in Table II, the reduced-order model [25] in Fig. 4 and (6) has the best overall performance and is recommended for the closed-loop controller design in normal applications, due to its simplicity and good conformity to the simulation results. For high-frequency DAB where the ZVS intervals have a significant impact on dynamics, the discrete-time model may be a better choice. Also

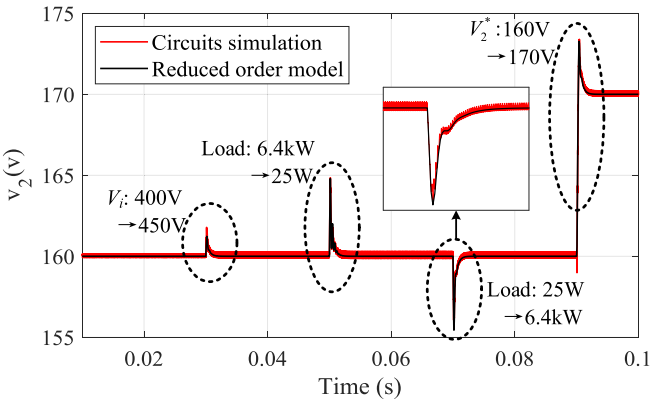

Fig. 13. Simulation results of the DAB output voltage v_2 with DAB circuit and the reduced-order model.

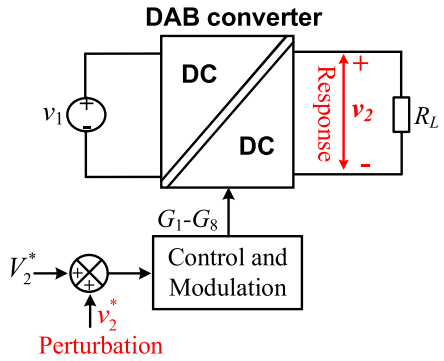

Fig. 14. Closed-loop transfer function evaluation circuit.

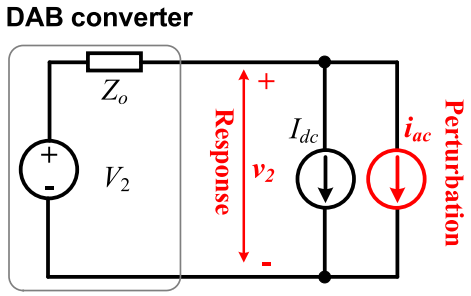

Fig. 15. Output impedance evaluation circuit.

note that the reduced-order model, generalized average model, and discrete-time model can be applied to a DAB modulated with DPS or TPS, and the related computation is more complex than that of the SPS.

The aforementioned analysis and simulation results suggest that the DAB is a first-order system, and the inductor L does not affect the DAB dynamic response. This interesting phenomenon may be explained as follows. The bipolar square voltages v_{ab} and v_{cd} of a DAB only have switching frequency f_s and its harmonics, and their dc components are 0, as shown in Figs. 2 and 3. The low-frequency component (below $f_s/2$) of the inductor current i_L, for instance, the envelope in Fig. 46, cannot be transferred to dc side because of the orthogonality relations

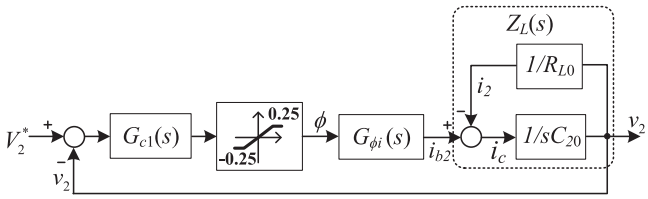

Fig. 16. Block diagram of feedback-only control.

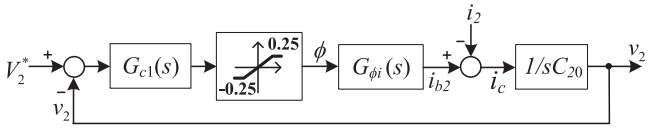

Fig. 17. Block diagram to obtain the output impedance of the feedback-only control.

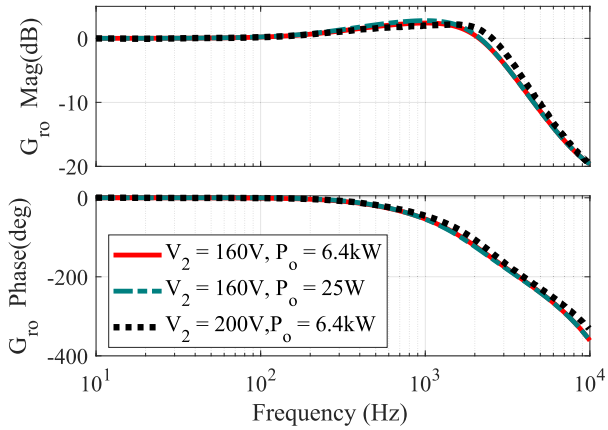

(a)

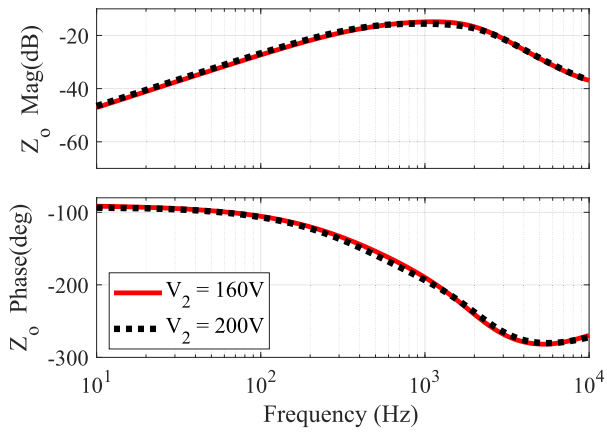

(b)

Fig. 18. Bode plot of the feedback-only control. (a) $G_{ro}(s)$ under different load conditions. (b) $Z_o(s)$.

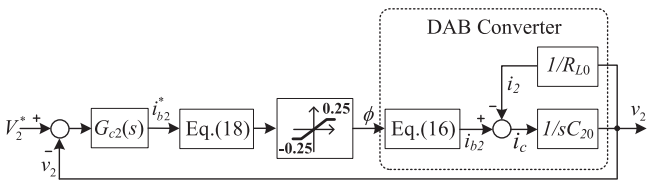

Fig. 19. Block diagram of the linearization control with resistive load [45].

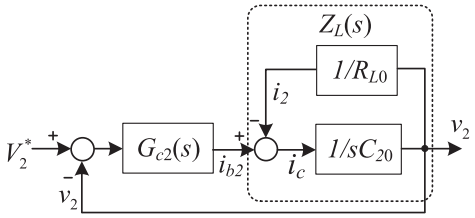

Fig. 20. Equivalent block diagram of the linearization control with resistive load.

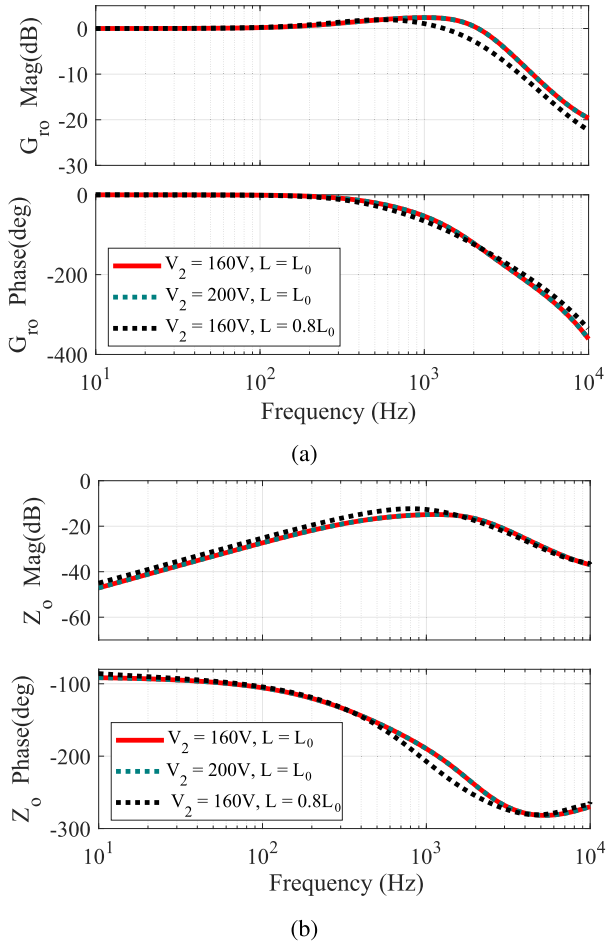

Fig. 21. Bode plot of the linearization control. (a) $G_{ro}(s)$. (b) $Z_o(s)$.

of the trigonometric functions

$$\int_t^{t+T_s} \sin(n \cdot 2\pi f_s t + \phi_1) \cdot \sin(\omega_L t + \phi_2) dt = 0 \ \ (2n\pi f_s \neq \omega_L) \tag{11}$$

where ω_L is the low-frequency component of i_L. As a result, the perturbation of i_L caused by disturbance such as change of the input voltage or phase-shift ratio cannot be propagated to output side, and the inductor L does not affect the DAB dynamic response. To further validate the aforementioned analysis, Fig. 13 shows simulation results of the DAB output voltage v_2 with the DAB circuit and the reduced-order model (see Fig. 4), where the DAB is controlled using the feedback-only control and the

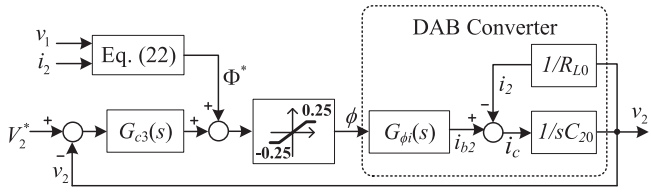

Fig. 22. Block diagram of the output current OCFF control.

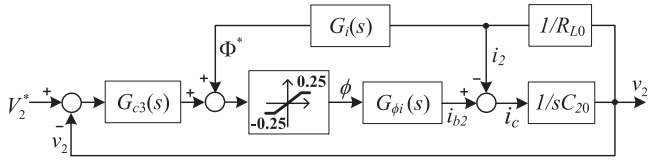

Fig. 23. Equivalent block diagram of the OCFF control.

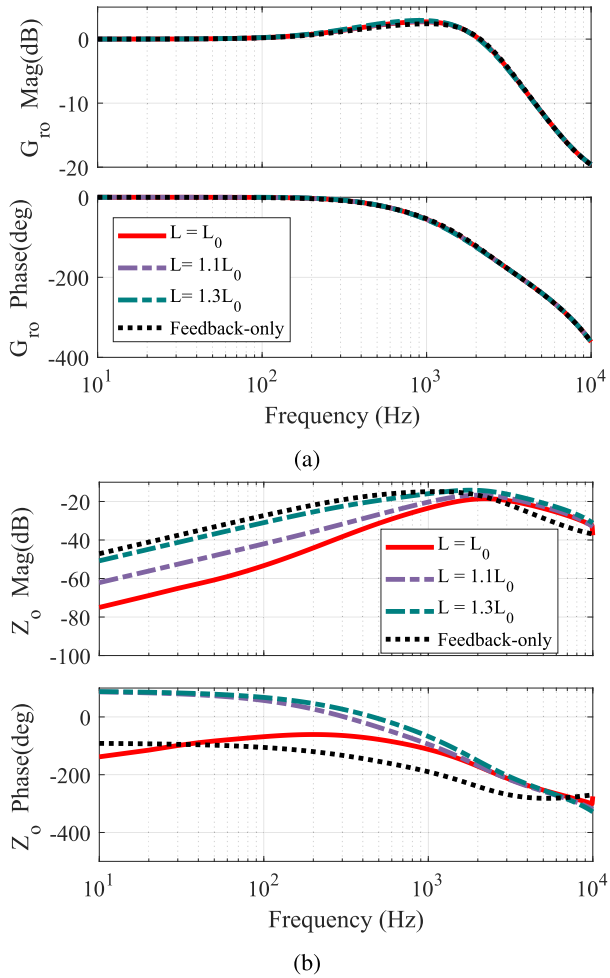

Fig. 24. Bode plot of the OCFF control. (a) $G_{ro}(s)$. (b) $Z_o(s)$.

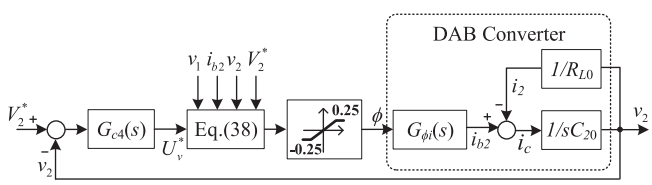

Fig. 25. Block diagram of the VDPC control [48].

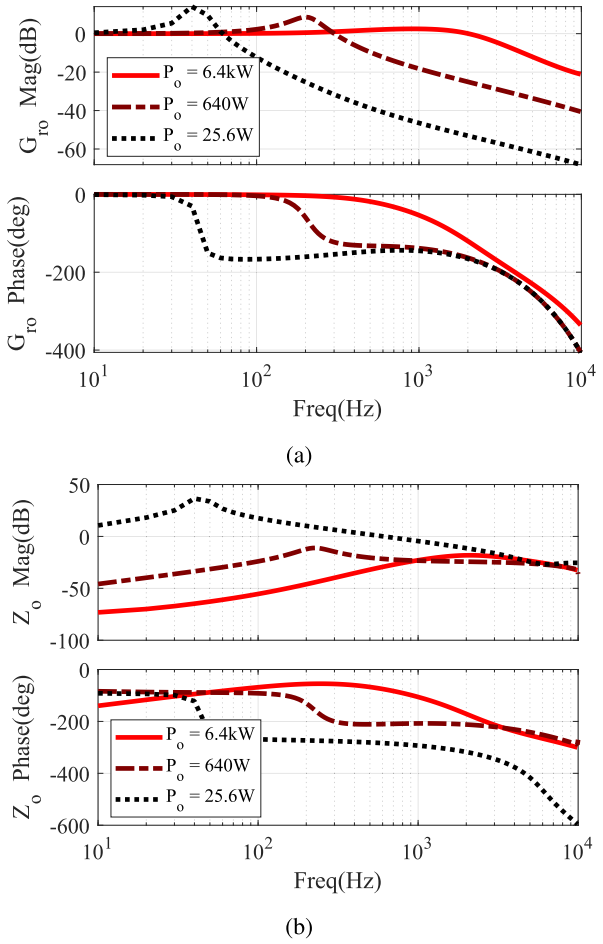

Fig. 26. Bode plot of the VDPC control. (a) $G_{ro}(s)$. (b) $Z_o(s)$.

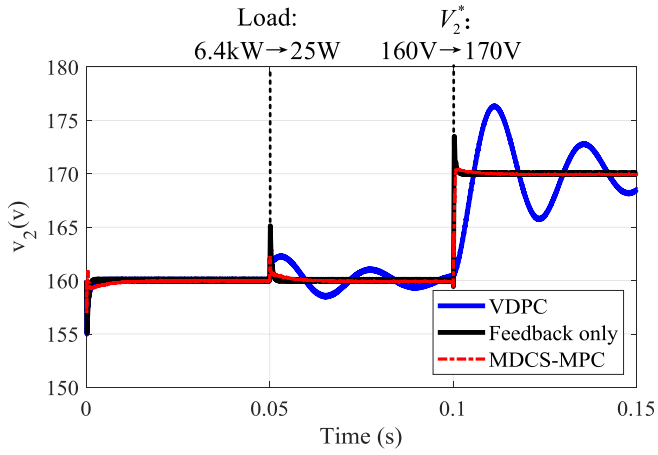

Fig. 27. Time-domain simulation results of the VDPC, feedback-only, and MDCS-MPC [48].

control parameters are listed in Table III. Under step change of the input voltage, load, and output reference, the reduced-order model predicts the DAB dynamic performance well.

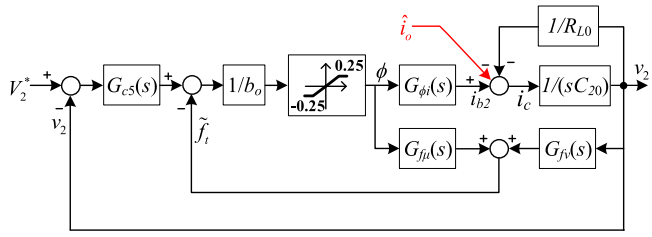

Fig. 28. Block diagram of the DOBC [50].

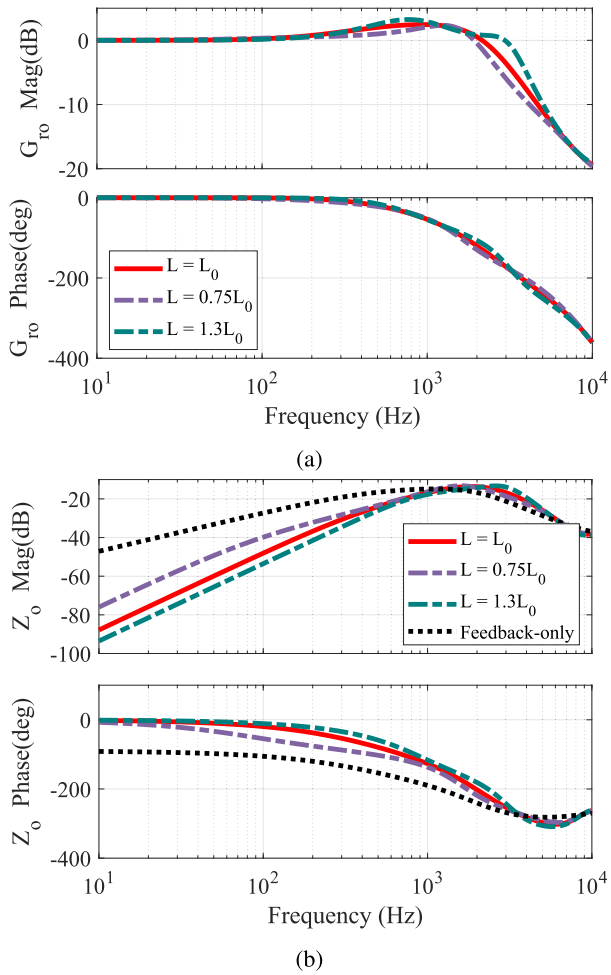

Fig. 29. Bode plot of the DOBC control. (a) $G_{ro}(s)$. (b) $Z_o(s)$.

III. Control of a DAB

This section mainly reviews the available output voltage control methods including the conventional feedback control, linearization control, feedforward plus feedback control, DOBC, FFCC, predictive current control, SMC, and model predictive control.

To effectively evaluate and compare these output voltage control methods, the closed-loop control-to-output transfer function $G_{ro}(s)$ and the output impedance $Z_o(s)$ are selected as the metrics of the ability in voltage tracking and load current disturbance rejection. The transfer functions $G_{ro}(s)$ and $Z_o(s)$ of the feedback control, linearization control, and feedforward

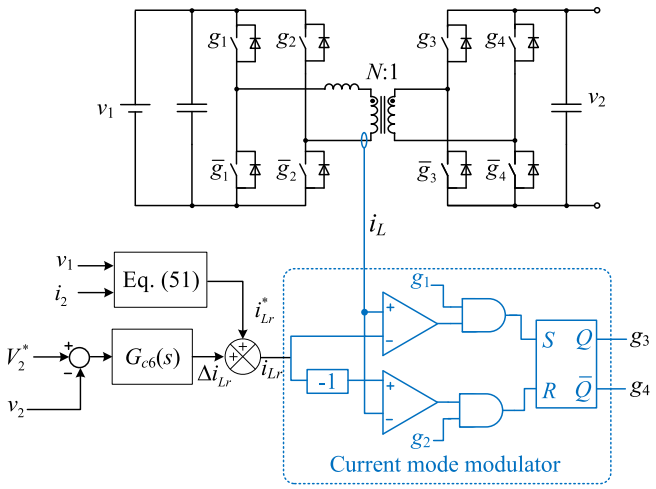

Fig. 30. Block diagram of the current mode control with feedforward of load current [53].

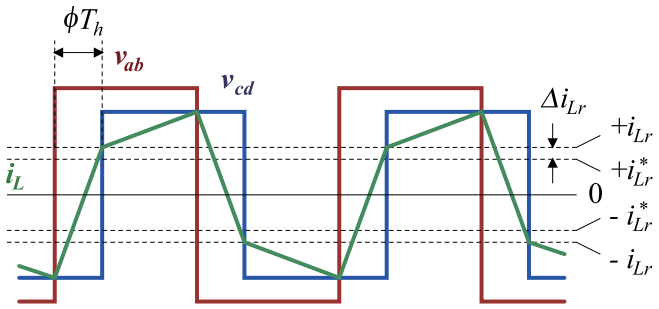

Fig. 31. Key waveforms of the current mode control in [53].

TABLE III
CONTROL PARAMETERS

Control Methods	Control Parameters
Feedback only, Fig. 16	$k_{p1} = 0.0193, k_{i1} = 37.6$
Linerization, Fig. 19 [45]	$k_{p2} = 7.3155, k_{i2} = 1.425 \times 10^4$
OCFF, Fig. 22	$k_{p3} = 0.0193, k_{i3} = 37.6$
VDPC, Fig. 25 [48]	$k_{p4} = 38.524, k_{i4} = 1.068 \times 10^5$
DOBC, Fig. 28 [50]	$k_{p5} = 7.53 \times 10^3, k_{i5} = 1.37 \times 10^7$
FFCC, Fig. 30 [53]	$k_{p6} = 4.35, k_{i6} = 3.17 \times 10^4$
Predictive current, Fig. 34 [56]	$k_{p7} = 24.8, k_{i7} = 1.45 \times 10^5$
SMC, Fig. 36 [64]	$k_{p8} = 7.3155, k_{i8} = 1.425 \times 10^4$
MDCS-MPC [68]	$\alpha_1 = 1, \alpha_2 = 0.5, \mu = 11,$ $\lambda = 1, V_m = 10V$

plus feedback control are derived theoretically, and frequency response plots based on the derived transfer function are provided. $G_{ro}(s)$ and $Z_o(s)$ plots of the FFCC, predictive current control, and mode predictive control are swept using simulation in Figs. 14 and 15.

In the reference to output ($G_{ro}(s)$) evaluation circuit (see Fig. 14), the reference signal consists of a dc component V_2^* and an a component v_2^*. V_2^* sets the equilibrium point, while

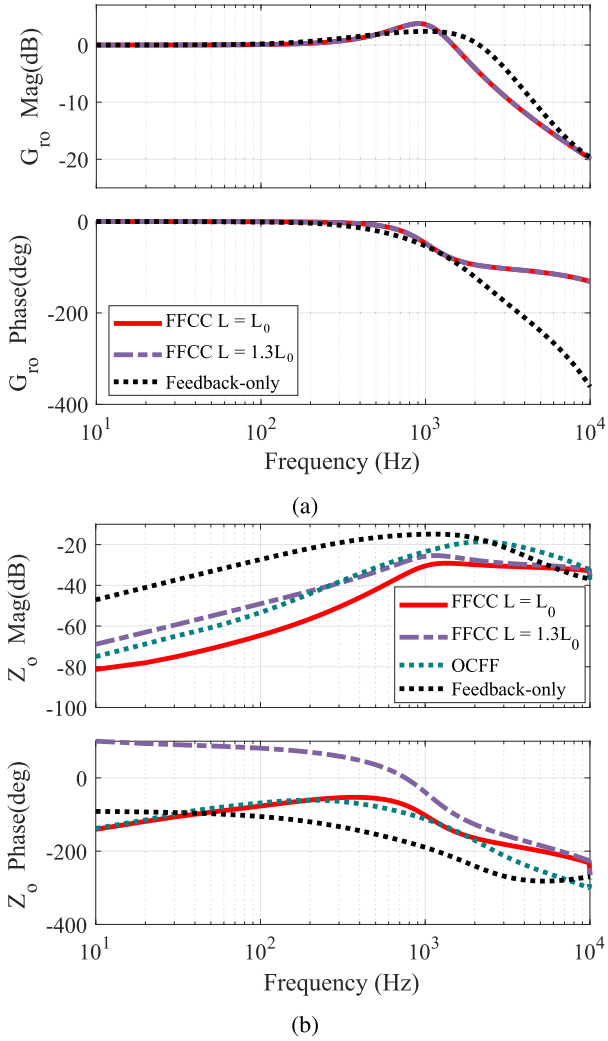

Fig. 32. Bode plot of the FFCC. (a) $G_{ro}(s)$. (b) $Z_o(s)$.

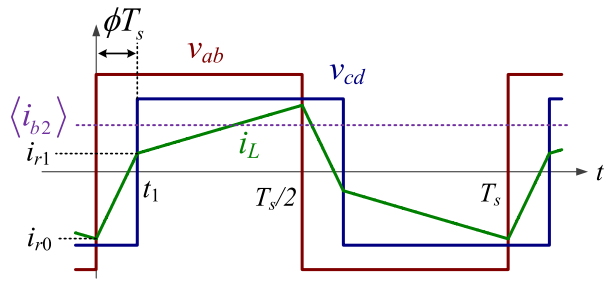

Fig. 33. DAB waveforms.

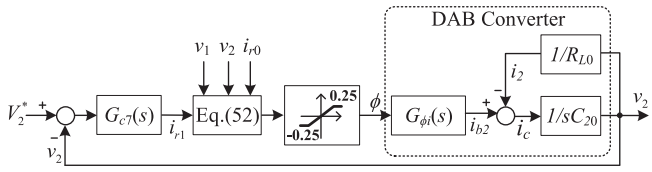

Fig. 34. Block diagram of the predictive current control [56], [57].

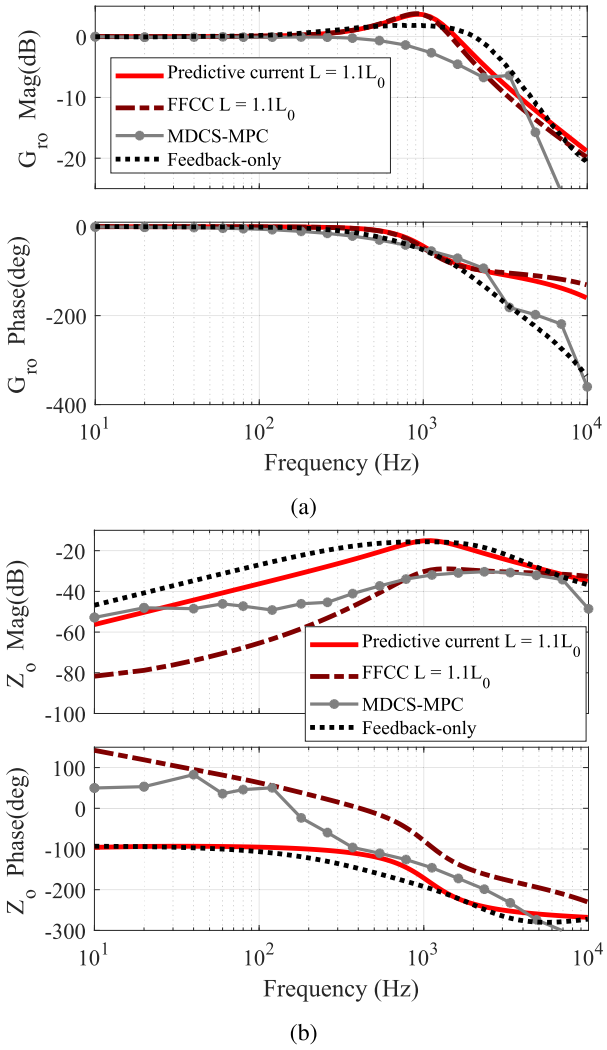

Fig. 35. Frequency response plot comparison of the predictive current control, FFCC, MDCS-MPC, and feedback-only control. (a) $G_{ro}(s)$. (b) $Z_o(s)$.

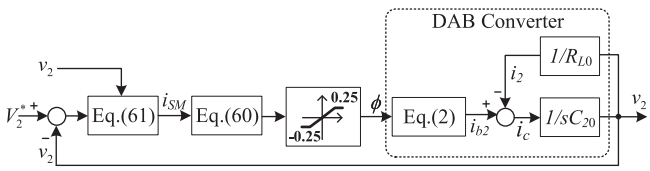

Fig. 36. Block diagram of the SMC [64].

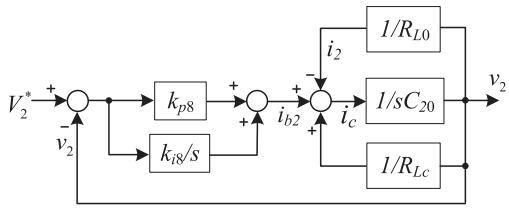

Fig. 37. Equivalent block diagram of the SMC with resistive load.

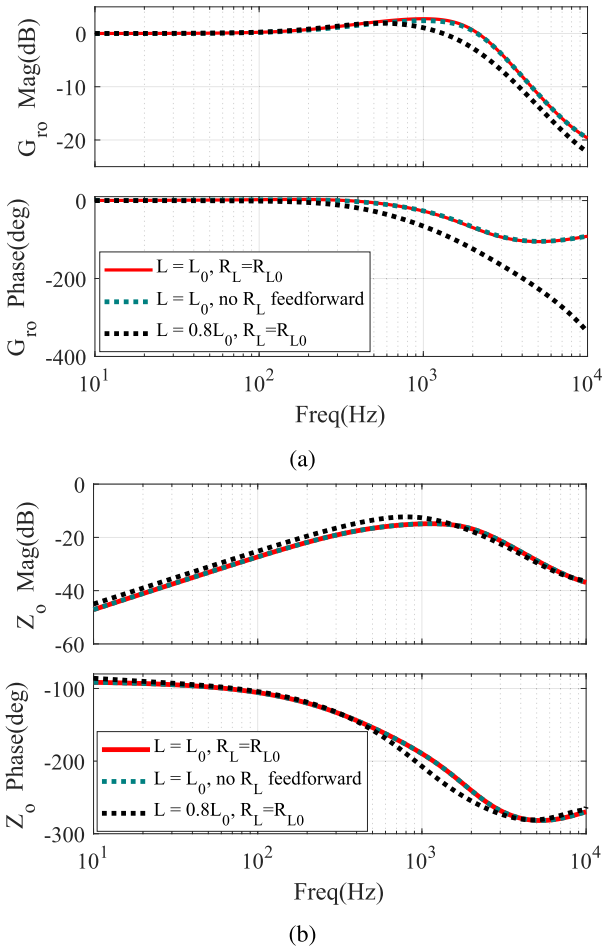

Fig. 38. Frequency response plot of the SMC. (a) $G_{ro}(s)$. (b) $Z_o(s)$.

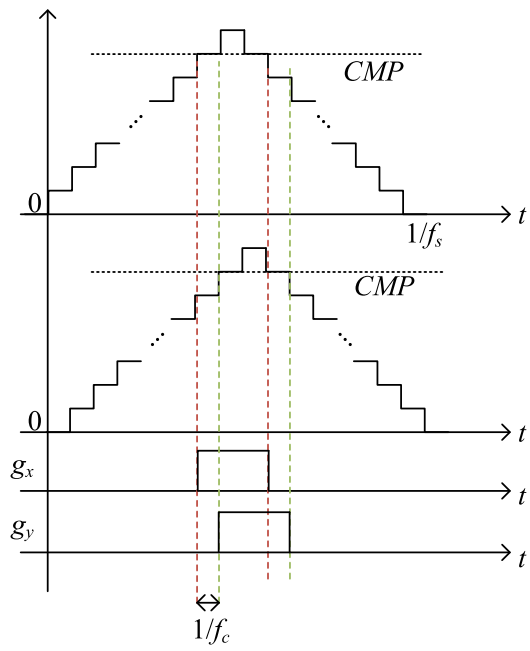

Fig. 39. Demonstration of the finest phase shift value in pulsewidth modulation modules [68].

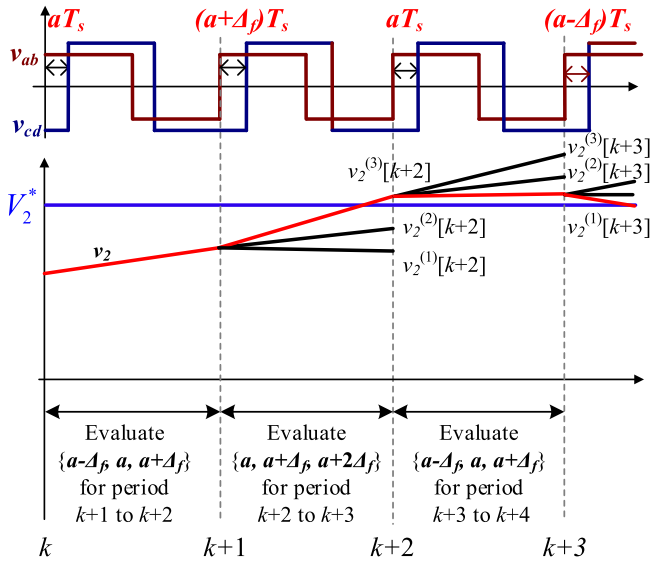

Fig. 40. Operating principle of MDCS-MPC and μ is set to be 3 for illustration [68].

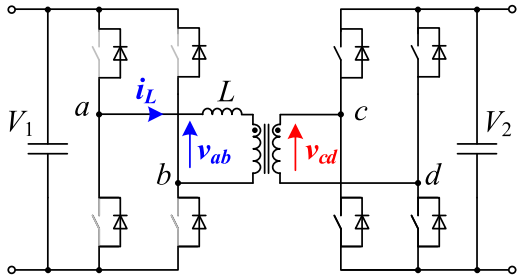

Fig. 41. Equivalent circuit of a DAB (modulated using the SPS) during the primary-side H-bridge dead time.

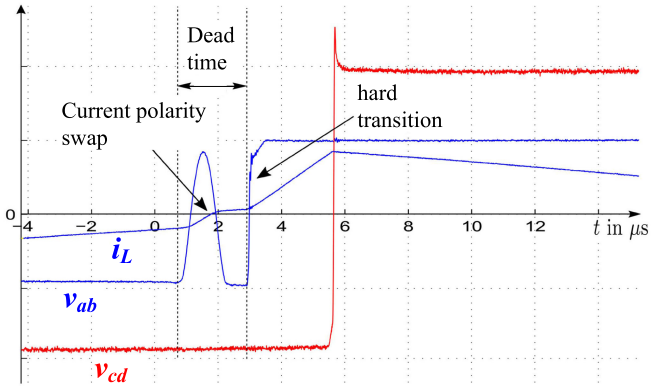

Fig. 42. Experimental waveforms: Voltage change polarity during the dead time [75].

v_2^* provides small-signal perturbation (sine wave at certain frequency). The output voltage v_2 of the DAB converter is measured at each frequency of the reference perturbation v_2^*. $G_{ro}(s)$ can be obtained by calculating the magnitude and phase difference between v_2^* and v_2 at each frequency

$$G_{ro}(f) = \frac{v_2(f)}{v_2^*(f)}. \tag{12}$$

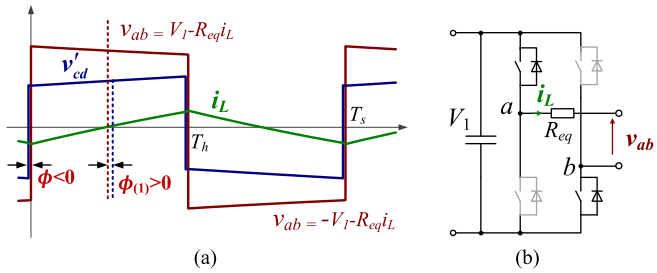

Fig. 43. Phase drift caused by voltage drop on components. (a) Waveforms. (b) Equivalent circuit when $0 < t < T_h$.

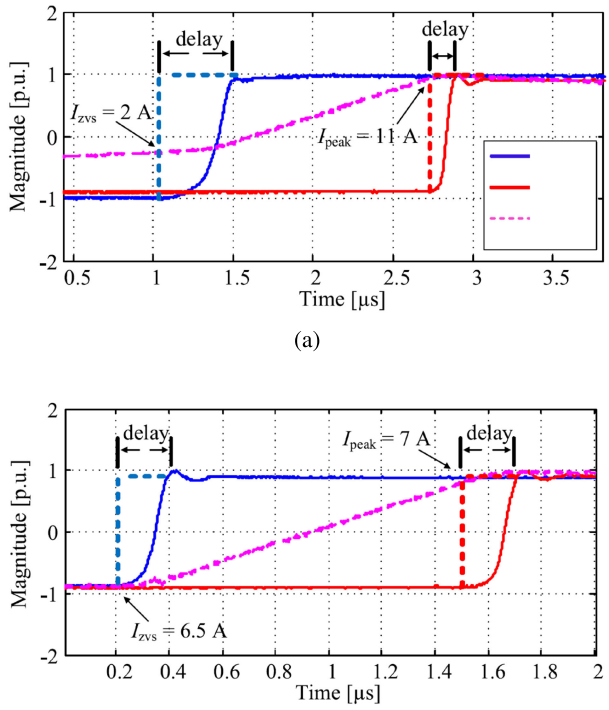

Fig. 44. Phase drift caused by switching current difference on the primary and secondary sides [76]. (a) $V_1 = 100$ V and $V_2 = 250$ V. (b) $V_1 = 130$ V and $V_2 = 250$ V.

In the output impedance ($Z_o(s)$) evaluation circuit (see Fig. 15), the DAB converter is simplified as a voltage source V_2 and an output impedance Z_o. $I_{\rm dc}$ represents the steady-state load current, which sets the equilibrium point, and $i_{\rm ac}$ stands for the injected small current that provides small-signal perturbation. The output voltage v_2 of the DAB converter is measured at each frequency of the injected current $i_{\rm ac}$. The output impedance can be obtained by calculating the magnitude and phase difference between v_2 and $i_{\rm ac}$ at each frequency

$$Z_o(f) = \frac{v_2(f)}{i_{\rm ac}(f)}. \tag{13}$$

The evaluation circuit in Figs. 14 and 15 can be easily implemented using PLECS Multitone Analysis tool or SIMetrix/SIMPLIS. Based on the frequency response plots, remarks for each control method are drawn.

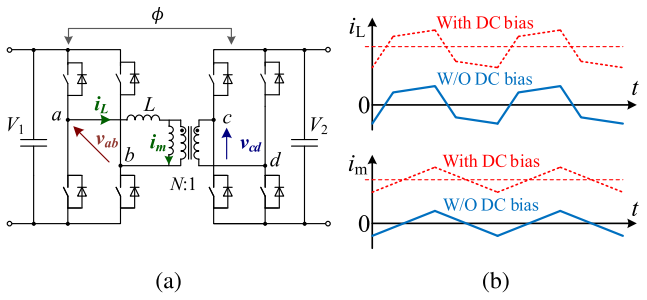

Fig. 45. Inductor current (i_L) and magnetizing current (i_m) with and without steady-state dc bias [77].

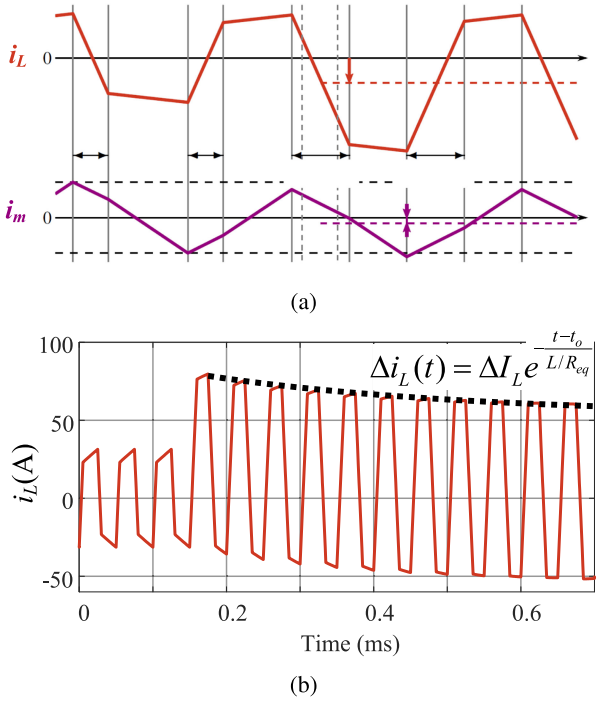

Fig. 46. (a) DC offset during the load transient. (b) Decay of dc offset over a time constant L/R_{eq} [78].

It is worth pointing out that the term "control method" here designates algorithms or circuits that takes only the sampling of the voltages and/or currents as inputs to generate the phase shift duties or active state duties of the DAB to track the output reference. By this definition, the so-called "control" in the literature [39]–[42] is classified as the optimization of advanced modulations rather than control methods discussed here.

A. Feedback Control on the Output Voltage

Feedback control with a proportional–integral (PI) compensator is the simplest method to regulate the output voltage. As shown in Fig. 16, the phase shift ratio ϕ between the primary and secondary bridges is modified dependent on the error in the output voltage [43], [44]. The PI compensator ($G_{c1}(s) = k_p + k_i/s$) is used to minimize the steady-state error.

Considering the delay in the digital controller, the closed-loop control-to-output transfer function is derived based on Fig. 16 as

$$G_{ro}(s) = \frac{v_2}{V_2^*} = \frac{G_{c1}G_{i\phi}Z_L e^{-1.5T_s s}}{1 + G_{c1}G_{\phi i}Z_L e^{-1.5T_s s}} \tag{14}$$

where $e^{-1.5T_s s}$ is the delay caused by the sampling and digital control. The sampling and control delays are T_s and $0.5T_s$, respectively. The digital control delay $0.5T_s$ is caused by that the control variable ϕ updates once per switching cycle. This process can be modeled as a zero-order hold (ZOH), whose delay is $0.5T_s$.

$Z_L(s)$ is shown in Fig. 16 and can be expressed as

$$Z_L(s) = \frac{R_L}{sC_2R_L + 1}. \tag{15}$$

To derive the output impedance $Z_o(s)$, the resistive load R_L is replaced with a current source i_2 in the DAB circuit as shown in Fig. 17. The output impedance can be developed as

$$Z_o(s) = \frac{v_2}{i_2} = -\frac{1/(sC_2)}{1 + G_{v1}G_{i\phi}e^{-1.5T_s s}/(sC_2)}. \tag{16}$$

The PI parameters are designed to achieve 1.2-kHz crossover frequency with 45° phase margin under full load ($R_L = 4\Omega$, $P_o = 6.4$ kW) and we obtain $k_{p1} = 0.0193$ and $k_{i1} = 37.6$. Fig. 18 shows the bode diagram of $G_{ro}(s)$ and $Z_o(s)$. Different load or output voltage conditions have minor influence on $G_{ro}(s)$ or $Z_o(s)$ as shown in Fig. 18.

B. Linearization Control

A linearized control method is proposed in [45] to eliminate the nonlinear terms in DAB. The control can reduce the sensitivity of the system stability to the load condition and reference voltage and help to enlarge the stable margin. Linearization control on the reduced-order model is considered.

According to (2), the relationship between ϕ and i_{b2} is nonlinear

$$\langle i_{b2} \rangle = \frac{NV_1\phi(1-2\phi)}{f_s L}. \tag{17}$$

By solving (17), we obtain

$$\phi = \begin{cases} \dfrac{1}{4} - \sqrt{\dfrac{1}{16} - \dfrac{f_s L i_2}{2NV_1}} & i_2 \geq 0 \\ -\dfrac{1}{4} + \sqrt{\dfrac{1}{16} + \dfrac{f_s L i_2}{2NV_1}} & i_2 < 0. \end{cases} \tag{18}$$

The control block diagram of the linearization control is shown in Fig. 19, where (18) is inserted into the control loop. Since (18) is the solution of (17), the nonlinearity of the control loop can be compensated. When the circuit parameters used in the control is exactly the same as that of the actual converter, then $i_{b2} = i_{b2}^*$ and Fig. 19 can be simplified as Fig. 20.

The reference to output transfer function is

$$G_{ro}(s) = \frac{G_{c2}Z_L e^{-1.5T_s s}}{1 + G_{c2}Z_L e^{-1.5T_s s}} \tag{19}$$

where $Z_L(s)$ is shown in (15). By replacing the resistor R_L with a current source (similar to that in Fig. 17), the output impedance

can be calculated as

$$Z_o(s) = -\frac{1}{sC_2 + G_{c2}e^{-1.5T_s s}}. \tag{20}$$

The PI parameters are designed to achieve 1.2-kHz crossover frequency with 45° phase margin under full load ($R_L = 4\Omega$) and we obtain $k_{p2} = 7.3155$ and $k_{i2} = 1.425 \times 10^4$. Fig. 21 shows the bode plot of the linearization control based on (19) and (20). Theoretically, $G_{ro}(s)$ and $Z_o(s)$ of the linearization control will not be affected by output voltage or load conditions. However, when the circuit parameters in (18) are different from the actual ones, for instance $L = 0.8L_0$, the bandwidth of the DAB becomes narrower. Note that L is the inductance used in the control, whereas L_0 is the inductance used in the actual DAB circuit (nominal value). Actually, according to Fig. 18, the closed-loop bandwidth and output impedance of the feedback-only control almost does not vary with different output voltage or load conditions, and the linearization may be not required.

C. Feedforward Plus Feedback Control on Output Voltage

Combined feedforward plus feedback control can improve the performance over simple feedback control as the disturbance can be measured and counterbalanced before it affects the process output.

1) Output Current Feedforward (OCFF): The relationship of the phase shift ratio ϕ and output power can be used as a feedforward term to minimize error between the actual and desired behavior. Based on (1), the desired output power can be expressed as

$$P_o^* = \frac{Nv_1v_2\Phi^*(1-2|\Phi^*|)}{f_sL}. \tag{21}$$

Therefore, the desired phase shift Φ^* can be calculated as

$$\Phi^* = \begin{cases} \frac{1}{4} - \sqrt{\frac{1}{16} - \frac{f_sLi_2}{2Nv_1}} & i_2 \geq 0 \\ -\frac{1}{4} + \sqrt{\frac{1}{16} + \frac{f_sLi_2}{2Nv_1}} & i_2 < 0. \end{cases} \tag{22}$$

Fig. 22 shows the control diagram, which is termed as OCFF control in this article. Alternatively Φ^* can be generated using a lookup table [32].

To derive the transfer functions of $G_{ro}(s)$ and $Z_o(s)$, it is necessary to linearize (22) using small-signal analysis. Assume the input voltage remains constant, local linearization of (22) yields

$$G_i(s) = \frac{d\Phi^*}{di_2} = \begin{cases} \frac{f_sL}{4NV_1}\left(\frac{1}{16} - \frac{f_sLI_2}{2NV_1}\right)^{-\frac{1}{2}} & I_2 \geq 0 \\ \frac{f_sL}{4NV_1}\left(\frac{1}{16} + \frac{f_sLI_2}{2NV_1}\right)^{-\frac{1}{2}} & I_2 < 0 \end{cases} \tag{23}$$

where I_2 is the equilibrium value calculated as

$$I_2 = \frac{NV_1\Phi(1-2\Phi)}{f_sL}. \tag{24}$$

With the feedforward gain $G_i(s)$, the control block diagram of Fig. 22 can be transformed to Fig. 23. The closed-loop control-to-output transfer function $G_{ro}(s)$ is derived based on Fig. 23 as

$$G_{ro}(s) = \frac{G_{c3}G_{i\phi}Z_Le^{-1.5T_s s}}{1 + (G_{c3}G_{i\phi} - G_iG_{i\phi}/R_L)Z_Le^{-1.5T_s s}} \tag{25}$$

where $Z_L(s)$ is shown in (15). To derive the output impedance, the resistive load R_L in Fig. 23 is replaced with a current source (similar to the transformation from Fig. 16 to Fig. 17). The output impedance of the OCFF control can be calculated as

$$Z_o(s) = \frac{(G_iG_{i\phi}e^{-1.5T_s s} - 1)/(sC_2)}{1 + G_{c3}G_{i\phi}e^{-1.5T_s s}/(sC_2)}. \tag{26}$$

Based on (3) and (23), when the circuit parameters used in the control are exact the same as the actual ones ($L = L_0$), we can calculate

$$G_iG_{\phi i} = 1. \tag{27}$$

Ignore the control delay $e^{-1.5T_s s}$ and substitute (27) into (25) and (26), we obtain

$$G_{ro}(s) = \frac{G_{c3}G_{i\phi}}{sC_2 + G_{c3}G_{i\phi}} \tag{28}$$

$$Z_o(s) = 0. \tag{29}$$

In (28), the feedforward term $G_i(s)$ eliminates the influence of R_L on $G_{ro}(s)$. In (29), the output impedance $Z_o(s)$ becomes zero with the feedforward gain G_i, indicating the perfect load disturbance rejection capability. However, the results in (28) and (29) are valid only when the circuit parameters used in the control are exact the same as the actual ones.

Assume L used in the control is $1/\alpha$ times of actual inductance L_0 as

$$L = L_0/\alpha. \tag{30}$$

Based on (4), (23), and (30), when $I_2 > 0$, the transfer function $G_i(s)$ becomes

$$G_i(s) = \frac{d\Phi^*}{di_2} = \frac{f_sL}{4\alpha NV_1}\left(\frac{1}{16} + \frac{\Phi^2 - \Phi/2}{\alpha}\right)^{-\frac{1}{2}} \tag{31}$$

where Φ is the quiescent value of ϕ shown in (4).

Multiplying (3) to (31), we calculate

$$G_{\phi i}G_i = \frac{(1-4\Phi)}{\alpha}\left(1 + \frac{16\Phi^2 - 8\Phi}{\alpha}\right)^{-0.5} \neq 1 \ \ (\text{when } \alpha \neq 1). \tag{32}$$

The PI parameters are designed to achieve 1.2-kHz crossover frequency with 45° phase margin under full load ($R_L = 4\Omega$) and we obtain $k_{p3} = 0.0193$ and $k_{i3} = 37.6$. Fig. 24 shows the bode plots of $G_{ro}(s)$ and $Z_o(s)$ of the OCFF control based on (25) and (26). As shown in Fig. 24(b), when $L = L_0$, the magnitude of Z_o of the OCFF control is much smaller than that of the feedback-only control. However, when $L = 1.1L_0$, the magnitude of $Z_o(s)$ increases; when $L = 1.3L_0$, the magnitude of $Z_o(s)$ becomes the same as that of the feedback-only control.

The results in Fig. 24 tell that the OCFF control needs the accurate acquisition of the circuit parameters in order to achieve a good load disturbance rejection. The practical performance

of the OCFF control may not be as good as designed. Similar methods are also found in [46] and [47].

2) Virtual Direct Power Control (VDPC): Another feedforward control termed as VDPC has been proposed in [48]. The advantage of the VDPC is that it eliminates the necessity of using the information of the inductance L by using the unified power to calculate Φ^*.

In this method, a virtual power reference p^* is defined as

$$p^* = |U_v^*| i_2^* \tag{33}$$

where $|U_v^*|$ is named as the virtual desired output voltage, which is the output value of the PI compensator in Fig. 25. Assuming a resistive load, the desired output current i_2^* can be described as

$$\frac{i_2^*}{V_2^*} = \frac{i_2}{v_2}. \tag{34}$$

Substituting i_2^* from (34) into (33) yields

$$p^* = \frac{|U_v^*| V_2^*}{v_2} i_2. \tag{35}$$

On the other hand, the unified power is expressed as

$$P_{\text{pu}} = P_o / P_{\text{base}} = V_1 v_2 \phi (1 - 2|\phi|) \tag{36}$$

where the unity base is

$$P_{\text{base}} = 1/(f_s L). \tag{37}$$

Let $P_{\text{pu}} = p^*$, we can calculate

$$\phi = \begin{cases} \dfrac{1}{4} - \sqrt{\dfrac{1}{16} - \dfrac{V_2^* U_v^* i_2}{4 v_2^2 v_1}} & i_2 \geq 0 \\ -\dfrac{1}{4} + \sqrt{\dfrac{1}{16} + \dfrac{V_2^* |U_v^*| i_2}{4 v_2^2 v_1}} & i_2 < 0. \end{cases} \tag{38}$$

In essence, the VDPC utilizes the virtual voltage U_v^* to avoid involving any circuit parameters such as the switching frequency f_s, inductance L, or transformer turn ratio N. The circuit parameter uncertainty has no influence on the control loop theoretically.

Similar to the OCFF control method, the closed-loop reference to output transfer function $G_{ro}(s)$ and output impedance $Z_o(s)$ can be calculated. The PI parameters are designed as $k_{p4} = 38.524$ and $k_{i4} = 1.068 \times 10^5$. Fig. 26 shows the bode plot of $G_{ro}(s)$ and $Z_o(s)$.

However, the VDPC can have a poor dynamic performance under light-load conditions. Under the light-load condition, i.e., $i_2 \approx 0$, the output of (38) is close to 0 and the VDPC loop gain will be small since (38) is inside the control loop. Fig. 26 shows the bode plot of $G_{ro}(s)$ and $Z_o(s)$ under different load conditions. Under the condition $P_o = 25\,\text{W}$, the control bandwidth drops significantly [see Fig. 26(a)]. As a result, the output impedance increase significantly [see Fig. 26(b)]. The narrow bandwidth and high output impedance indicate a poor performance on voltage tracking and load current disturbance rejection. The aforementioned observation is further validated using the time-domain simulation results in Fig. 27. When the load steps to light at 0.05 s, the dynamic performance becomes poor.

D. Disturbance-Observer-Based Control (DOBC)

In the aforementioned feedforward control methods, the OCFF control can significantly reduce the output impedance and improve the load disturbance rejection capability. However, its performance deteriorates quickly in the presence of parameter uncertainty. The VDPC tries to solve the parameter sensitivity problem by using the PI output to estimate the phase shift, but its loop gain is too low under light-load conditions. Besides, an additional current sensor is required in these feedforward control methods.

Disturbances and uncertainties exist in all power converter control systems [49]. These disturbances and uncertainties include input voltage and load variation, model uncertainty, and circuit parameter variations due to temperature or aging effects [50]. DOBC employs an observer to estimate the total disturbances and uncertainties, and the corresponding compensation is then generated by making use of the estimate [49]. Therefore, the DOBC can achieve superior control performance. The input to the disturbance observer is the output voltage v_2 and control signal (phase shift ratio ϕ), no additional current sensor is required [50], [51].

DOBC for the DAB converter has been introduced in [50]–[52]. The derivation procedures of the disturbance observer from [50] are briefly repeated here to illustrate its basic principles.

According to Fig. 4, we can obtain the following small-signal equation:

$$\frac{d\hat{v}_2}{dt} = \frac{N V_1 (1 - 4\Phi)}{f_s L C_2} \hat{\phi} - \frac{\hat{v}_2}{R_L C_2}. \tag{39}$$

Rearrange (39), we can get

$$\frac{d\hat{v}_2}{dt} = f_t \left(\hat{v}_2, \hat{\phi} \right) + b_0 \hat{\phi} \tag{40}$$

where $f_t(\hat{v}_2, \hat{\phi}) = a\hat{v}_2 + (b - b_0)\hat{\phi}$ is the total disturbance, which includes external disturbances, circuit parameter variations, and model uncertainties, with

$$a = -\frac{1}{R_L C_2}, b = \frac{N V_1 (1 - 4\Phi)}{f_s L C_2}, b_0 = \frac{N V_{10} (1 - 4\Phi_0)}{f_s L_0 C_{20}}$$

where V_{10}, L_0, and C_{20} are the nominal values of the input voltage, inductance, and output capacitance, respectively.

The disturbance observer for the DAB can be designed as follows:

$$\frac{d\tilde{\hat{v}}_2}{dt} = \tilde{f}_t + \beta_1 \left(\hat{v}_2 - \tilde{\hat{v}}_2 \right) + b_0 \hat{\phi} \tag{41}$$

$$\frac{d\tilde{f}_t}{dt} = \beta_2 \left(\hat{v}_2 - \tilde{\hat{v}}_2 \right) \tag{42}$$

where $\tilde{\hat{v}}_2$ and $\tilde{f}_t$ are the estimated values of $\hat{v}_2$ and f_t, respectively.

Define the estimation error $e_1 = \hat{v}_2 - \tilde{\hat{v}}_2$ and $e_2 = f_t - \tilde{f}_t$, then the following equations can be derived considering (40)–(42):

$$\begin{cases} \dot{e}_1 = e_2 - \beta_1 e_1 \\ \dot{e}_2 = \dot{f}_t - \beta_2 e_1. \end{cases} \tag{43}$$

By choosing β_1 and β_2 positive, then e_1 and e_2 converge to zero exponentially, i.e., the estimated states will converge to the actual states [50].

Choose $\beta_1 = 2\zeta\omega_n$ and $\beta_2 = \omega_n^2$. Rearrange the disturbance observer (41) and (42) as follows:

$$\dot{\mathbf{X}} = \mathbf{A}\mathbf{X} + \mathbf{B}\mathbf{U} \tag{44}$$

where

$$\mathbf{X} = \begin{bmatrix} \tilde{\hat{v}}_2 \\ \tilde{f}_{\rm t} \end{bmatrix} \mathbf{A} = \begin{bmatrix} -2\zeta\omega_n & 1 \\ -\omega_n^2 & 0 \end{bmatrix}$$

$$\mathbf{B} = \begin{bmatrix} b_{\rm o} & 2\zeta\omega_n \\ 0 & \omega_n^2 \end{bmatrix} \mathbf{U} = \begin{bmatrix} \hat{\phi} \\ \hat{v}_2 \end{bmatrix}.$$

From (44), the transfer functions from ϕ and v_2 to $\tilde{f}_t$ can be derived as follows:

$$G_{f\mu}(s) = \frac{\tilde{f}_t}{\hat{\phi}} = \frac{-\omega_n^2 b_o}{s^2 + 2\zeta\omega_n s + \omega_n^2} \tag{45}$$

$$G_{fv}(s) = \frac{\tilde{f}_t}{\hat{v}_2} = \frac{\omega_n^2 s}{s^2 + 2\zeta\omega_n s + \omega_n^2}. \tag{46}$$

Fig. 28 shows the block diagram of the DOBC. The estimated disturbance $\tilde{f}_t$ is subtracted to compensate the actual disturbance in the control system. Loop gain of the control system can be calculated as

$$G_o(s) = \frac{G_{c5}(s)G_{\phi i}Z_L e^{-1.5T_s s} b_o^{-1}}{1 + (G_{fv}G_{\phi i}Z_L + G_{f\mu})e^{-1.5T_s s} b_o^{-1}}. \tag{47}$$

The PI parameters of $G_{c5}(s)$ are designed to achieve 1.2-kHz crossover frequency with 45° phase margin under full load ($R_L = 4\Omega$). When $L = L_0$ and $C_2 = C_{20}$, we obtain $k_{p5} = 7.53 \times 10^3$ and $k_{i5} = 1.37 \times 10^7$. These control parameters are large because of the gain $1/b_o$ in the control loop in Fig. 28, where $b_o = 3 \times 10^5$ in this design. After multiplying this gain, the PI parameters of DOBC are of the same order of magnitude of that of other control methods.

The output impedance can be calculated as follows:

$$Z_o(s) = \frac{-1}{sC_2 + (G_{c5} + G_{fv})\dfrac{e^{-1.5T_s s} b_o^{-1}}{1 + G_{f\mu}e^{-1.5T_s s} b_o^{-1}} G_{\phi i}}. \tag{48}$$

Fig. 29 shows the bode plots of $G_{ro}(s)$ and $Z_o(s)$ of the DOBC based on (47) and (48). According to Fig. 29(b), the output impedance of the DOBC is much smaller than that of the feedback-only control, indicating better load disturbance rejection capability. Besides, the performance of the DOBC is not sensitive to the parameter variation. These superior performance is due to the load disturbance and parameter uncertainties are estimated and compensated by the disturbance observer in the DOBC.

E. Current Mode Control

The common feature of this category is that the transformer current is involved in the control. The information of the transformer current can improve the dynamic performance and provide a way to limit the peak transformer current.

1) Feedforward Current Control (FFCC): A FFCC is introduced by Shan *et al.* [53] with the transformer instant current being regulated similar to the peak current control in [54]. The control block diagram when the power transfer from the primary to secondary side is shown in Fig. 30 and typical waveforms are shown in Fig. 31. With an SR flip–flop, the secondary bridge is commutated at the time instant when the transformer current is equal to a reference i_{Lr} (see Figs. 30 and 31).

The inductor current i_L changes from i_{Lr} to $-i_{Lr}$ from time ϕT_s to $(1/2 + \phi)T_s$, therefore

$$i_{Lr} = \frac{Nv_2 - v_1(1 - 4\phi)}{4f_s L}. \tag{49}$$

According to (2) and (49), we calculate

$$i_{Lr} = \frac{i_2}{N}\frac{2}{1 + \sqrt{1 - \dfrac{8i_2 L f_s}{v_1 N}}} - \frac{v_1 - Nv_2}{4Lf_s}. \tag{50}$$

Since the term $(v_1 - Nv_2)/(4Lf_s)$ has slower time variation and can be compensated using the feedback term Δi_{Lr} in Fig. 30, (50) can be simplified as

$$i_{Lr}^* = \frac{i_2}{N}\frac{2}{1 + \sqrt{1 - \dfrac{8i_2 L f_s}{V_1 N}}}. \tag{51}$$

With the FFCC, fast changes on i_2 or $V_2{}^*$ will lead to an immediate change at $i_{Lr}{}^*$ to enable a fast response. During the transient period, the inaccuracy on the feedforward algorithm is compensated by the PI feedback controller. Since the transformer current is directly manipulated, the transient dc-offset current on the DAB transformer can be inherently eliminated.

The open-loop bode plot of the FFCC (see Fig. 30) can be swept using PLECS multitone analysis tool. Based on the swept open-loop bode plot, the PI compensator for the FFCC are designed to achieve 1.2-kHz crossover frequency with 45° phase margin, and the resultant PI parameters are: $k_{p6} = 4.35$ and $k_{i6} = 3.17 \times 10^4$.

The bode plots of $G_{ro}(s)$ and $Z_o(s)$ of the FFCC are swept using the evaluation circuits (see Figs. 14 and 15) in the software PLECS. The swept $G_{ro}(s)$ and $Z_o(s)$ are shown in Fig. 32, where L_0 is the actual inductance in DAB and L is the inductance value used in the FFCC. With the feedforward term and current mode control, the output impedance of the FFCC is the smallest compared to feedback-only control and OCFF control. Besides, in the presence of the parameter variation, the performance of the FFCC control degrades less significantly compared to the OCFF control (see Fig. 24). Even when $L = 1.3L_0$, the output impedance of the FFCC is still much smaller than the feedback-only control.

Just like the other peak current control method, the FFCC is susceptible to noise. A noise spike is generated each time the power devices switch. The spike can be large when the DAB loses ZVS. A fraction of a volt coupled into the control circuit can cause the switch turn OFF immediately, resulting subharmonic operating mode with much greater ripple [55]. Possible solutions to suppress the sampling noise and to avoid subharmonic oscillations include the following:

1) operation of DAB in ZVS-ON region;
2) utilization of the isolated current sensor;
3) addition of the filter on the sampled current.

In addition, the logic circuit of the current mode modulator can be complex when the DAB operating bidirectionally.

2) Predictive Current Control: Another digital predictive current control is proposed by Dutta*et al.* [56], [57]. As shown in Fig. 33, the phase shift ϕ can be calculated as

$$\phi = \frac{i_{r1} - i_{r0}}{T_s} \frac{L}{v_1 + N v_2}. \tag{52}$$

With (52), the block diagram of the predictive current control is illustrated in Fig. 34. i_{r1} is generated by the compensator, whereas i_{r0}, v_1, and v_2 are sampled each switching cycle.

The open-loop bode plot of the predictive current control can be swept using the PLECS multitone analysis tool. Based on the swept results, the PI compensator for the predictive control is designed to achieve 1.2-kHz crossover frequency with 45° phase margin, the resultant PI parameters are $k_{p7} = 24.8$ and $k_{i7} = 1.45 \times 10^5$.

The bode plots of $G_{ro}(s)$ and $Z_o(s)$ of the predictive current control are swept using the evaluation circuits obtained using the software PLECS. The results are shown in Fig. 35. Parameter tolerance is considered $L = 1.1L_0$. The output impedance of the predictive current control is smaller than that of the feedback-only control, but higher than that of the FFCC.

The predictive current control requires ac current sampling and intensive computation in one switching period. For DAB converters with wide bandgap (WBG) devices where switching frequency could range from 100 kHz–1 MHz [15], [58], it is challenging to implement this predictive current control.

F. Sliding Mode Control (SMC)

Small-signal models and analysis have been widely used in the power electronics for the stability assessment. However, they fail to predict the stability of some converters in the presence of large transient. Worse still, the small-signal model fails to reveal any stability information of the converter over the entire operating region [59]. In [60] and [61], it is shown that even though stable operation is concluded from the small-signal analysis, the system can be unstable. The main advantage of a system with SMC is that it has guaranteed stability and robustness against parameter uncertainties [62].

The SMC has been applied to the DAB converter in [63] based on the generalized average model, and in [64], based on the reduced-order model. According to Section II, the reduced-order model presents better accuracy compared to the generalized average model, therefore the SMC is introduced with the reduced-order model.

In general, assume the dynamic equation of a system is

$$\frac{dx}{t} = f + gu \tag{53}$$

where x is the state variable, f and g are the functions of x, and u is the discontinuous control action expressed as

$$u = \begin{cases} U^+ & \text{if } S(x,t) > 0 \\ U^- & \text{if } S(x,t) < 0 \end{cases} \tag{54}$$

where U^+ and U^- are either scalar values or scalar functions of x. $S(x,t)$, usually called the sliding mode surface, is the instantaneous feedback tracking trajectory of the system and is predetermined function of the state variable [59]. Typically, $S(x,t)$ is chosen as a linear combination of weighted values of the state variables

$$S(x,t) = \sum_{i=1}^{m} \alpha_i x_i. \tag{55}$$

The ideal sliding mode action described in (54) is similar to the ON and OFF bang–bang control, which results in the high-frequency oscillation within the vicinity of the sliding surface while moving toward origin. Alternatively, equivalent control has been used to replace (54). The equivalent control action is obtained by solving the following. This is called the invariance condition [59].

$$\frac{dS(x,t)}{dt} = 0. \tag{56}$$

The steady-state error that occurs with the SMC (54) can be minimized by comprising an integral term of the state variable into the sliding surface [65]. This approach is called integral SMC. However, the integral SMC becomes less effective when equivalent control action is implemented [66]. Therefore, Tan *et al.* proposed an additional double integral term of the state variables for the construction of the sliding surface when the equivalent SMC is utilized [67].

In the DAB converter, state variables are chosen to be [64]

$$x = [x_1, x_2, x_3]^T = [v_{\text{err}}, \int_0^t v_{\text{err}} dt, \int_0^t x_2 dt]^T \tag{57}$$

where $v_{\text{err}} = V_2^* - v_2$.

According to Fig. 4 and (2), the state equation of the DAB can be written as

$$\frac{dv_2}{dt} = -\frac{v_2}{C_2 R_L} + \frac{v_1}{C_2 f_s L} \phi (1 - 2|\phi|). \tag{58}$$

According to the double integration approach [67], the sliding surface is constructed as

$$S(x,t) = \sum_{i=1}^{3} \alpha_i x_i. \tag{59}$$

According to the invariance condition (56), the equivalent control law can be derived as

$$\phi = \begin{cases} \frac{1}{4} - \sqrt{\frac{1}{16} - \frac{f_s L i_{\text{SM}}}{2v_1}} & i_{\text{SM}} \geq 0 \\ -\frac{1}{4} + \sqrt{\frac{1}{16} + \frac{f_s L i_{\text{SM}}}{2v_1}} & i_{\text{SM}} < 0 \end{cases} \tag{60}$$

i_{SM} used in (60) can be expressed as [64]

$$i_{\text{SM}} = \frac{v_2}{R_{Lc}} + C_2 \frac{\alpha_2}{\alpha_1} v_{\text{err}} + C_2 \frac{\alpha_3}{\alpha_1} \int_0^t v_{\text{err}} dt \tag{61}$$

where R_{Lc} is the load resistance value used in the control.

Different from (18), i_{SM} in (60) is a virtual current generated by (61). Based on (60) and (61), the SMC control diagram is shown in Fig. 36. Essentially, (61) is the PI compensator plus a feedforward term. Besides, (60) is the solution of (18), similar to the linearization control. Therefore, the SMC block diagram in Fig. 36 can be equivalent to Fig. 37, where $k_{p8} = C_2\alpha_2/\alpha_1$ and $k_{i8} = C_2\alpha_3/\alpha_1$.

Based on Fig. 37, the PI parameters of the SMC is designed to achieve a 1.2-kHz crossover frequency with 45° phase margin: $k_{p8} = 7.3155$ and $k_{i8} = 1.425 \times 10^4$, which is the same as that of the linearization control. Similar to the linearization control, the transfer functions of $G_{ro}(s)$ and $Z_o(s)$ can be derived according to Fig. 37. Fig. 38 shows bode plots of $G_{ro}(s)$ and $Z_o(s)$ of the SMC control. The feedforward term R_{Lc} actually does not affect $G_{ro}(s)$ or $Z_o(s)$, and the bode plots of the SMC are exact the same as that of the linearization control. When the inductance value L used in the control is different from the actual one (L_0) in the circuit, the control bandwidth becomes narrower and the output impedance increases.

G. Predictive Control on Output Voltage

The utilization of predictive controls on the DAB generally provides salient dynamic performance. They draw on the information of the circuit to calculate the optimal value for the future control variables.

A MDCS-MPC is proposed by Chen *et al.* [68], [69]. The phase shift ratio ϕ is divided into the discretized elements to fit digital control.

According to (1) and Fig. 5, the DAB output voltage is regulated by the phase shift ϕ, which is continuous in nature. To adapt digital control, ϕ needs to be discretized. Consider a commercial microcontroller with a peripheral clock f_c (see Fig. 39), the finest phase shift value Δ_f is

$$\Delta_f = \frac{f_c}{f_s} \tag{62}$$

where f_s is the DAB switching frequency.

The range of the DAB phase shift ratio is

$$\phi \in [-0.25, 0.25]. \tag{63}$$

The aforementioned ϕ can be further discretized into $\mu_m (= 1/\Delta_f + 1)$ elements as described in array

$$\phi \in \{-0.25, \ldots, 0, \Delta_f, 2\Delta_f, \ldots, 0.25\}. \tag{64}$$

Taking into account the computational delay, MDCS-MPC has a prediction horizon of two sampling periods. To illustrate the principle of MDCS-MPC, consider a cost function in (65) that only regulating the output voltage v_2 to the reference V_2^*

$$ct = ({V_2}^* - v_2[k+2])^2. \tag{65}$$

This cost function is executed during the time instant $[k, k+1]$ and $v_2[k+2]$ is the predicted output voltage at time instance $k+2$ and can be calculated based on Fig. 4 [68] as

$$v_2[k+2] = \frac{i_{b2}[k+1] + i_{b2}[k] - 2i_2[k]}{C_2 f_s} + v_2[k] \tag{66}$$

where $i_{b2}[k+1], i_{b2}[k]$ can be calculated using $\phi[k]$ (already known) and $\phi[k+1]$ (predicted) based on the reduced-order model (2). The error caused by power losses can be compensated using I_{comp} [28] as

$$I_{\text{comp}}[k] = i_{b2\_r}[k-1] - i_{b2}[k-1] \tag{67}$$

where i_{b2} is indicated in Fig. 10 and is calculated using the reduced-order model (2) (without power losses); and i_{b2_r} is calculated using the measured load current I_{load}, where the information of power losses is included

$$i_{b2\_r}[k-1] = \frac{C_2}{T_s}\left(v_2[k] - v_2[k-1]\right) + I_{\text{load}}[k-1]. \tag{68}$$

Fig. 40 shows how to choose ϕ in the next switching cycle. In the control interval k to $k+1$, when $\phi[k+1]$ equals to $a - \Delta_f$, a, and $a + \Delta_f$, the output voltage v_2 is predicted as $v_2^{(1)}[k+2], v_2^{(2)}[k+2]$ and $v_2^{(3)}[k+2]$, respectively, based on (2) and (66). As shown in Fig. 40, when $\phi[k+1] = a + \Delta_f$, the predicted output voltage $v_2^{(3)}[k+2]$ is the closest to V_2^*. This results in the smallest cost function defined in (65). Therefore, the value $a + \Delta_f$ is applied to ϕ at time instance $k+1$. In the next control interval, the same process is repeated. However, the moving discretized control set has changed and become $\{a, a + \Delta_f, a + 2\Delta_f\}$, centered at the previous working point $\phi[k+1] = a + \Delta_f$. In this control interval, $\phi[k+2] = a$ results in a smallest cost function.

In the aforementioned example, $\mu = 3$ points are assessed in each switching cycle, larger value of μ can increase the transition dynamics, but it aggravates the computational burden to the real-time digital controller. Therefore, an adaptive step for ϕ is adopted instead of the finest search step Δ_f. Define the adaptive step Δ_{adp} as (70). The adaptive step Δ_{adp} changes with the deviation of the output voltage to the reference. When v_2 is far from the reference, Δ_{adp} grows large. In contrast, when v_2 equals to the reference, Δ_{adp} becomes Δ_f. Such that, the control accuracy remains

$$V_\Delta = \begin{cases} |{V_2}^* - v_2[k]|, & |{V_2}^* - v_2[k]| < V_m \\ V_m, & |{V_2}^* - v_2[k]| > V_m \end{cases} \tag{69}$$

$$\Delta_{\text{adp}} = \Delta_f(1 + \lambda {V_\Delta}^2) \tag{70}$$

where V_m is the saturated voltage and λ is a coefficient determined according to the requirement of transition performance.

To provide damping and enhance the resistance to analogue to digital sampling noise in practice, the cost function can be modified as follows:

$$ct = \alpha_1 G_1 + \alpha_2 G_2 \tag{71}$$

where

$$\begin{cases} G_1 = ({V_2}^* - v_2[k+2])^2 \\ G_2 = (v_2[k+2] - v_2[k])^2. \end{cases} \tag{72}$$

The first term G_1 is responsible for the regulation of the output voltage v_2 to reference value V_2^*, while the second term G_2 takes charge of the voltage deviation reduction. When v_2 is far from the reference value, G_1 plays a dominant role in the cost function. However, when v_2 reaches close to V_2^*, G_2 starts to take effect.

TABLE IV
COMPARISON OF DAB CONTROL METHODS

Control Methods	Implementation complexity	Dynamic performance	Robustness against parameter variation	Implementation cost	Other comments
Feedback only	Low	++	+++	Low, 1 sensor	
Feed-forward	Medium	++++	++	Medium, 3 sensors	
VDPC	Medium	+++	+	Medium, 3 sensors	Poor steady-state and dynamic performance under light load conditions
DOBC	Medium	++++	++++	Medium, 1 sensor	
FFCC	High	++++	+++	High, 3 sensors	Can be affected by the switching noise (similar to peak current mode control).
Predictive current control	Medium	++++	++	Medium, 3 sensors	Not suitable for high frequency applications.
SMC	Low	++	++	Low, 1 sensor	
MDCS-MPC	High	++++	++	High, 3 sensors	The control parameters have a significant impact on the control performance, these control parameters are chosen based on trial and error or the machine learning.

Note: **+ = Poor**; **++ = Average**; **+++ = Good**; **++++ = Excellent**

G_2 puts constraint on variation of v_2. This essentially prevents v_2 from dithering due to analog-to-digital sampling noise. G_2 also alleviates the oscillation during load transitions. More terms can be added to the cost function to achieve multiple control objectives [70].

The development of the analytical small-signal model of DAB converters with MDCS-MPC is infeasible. The small-signal evaluation circuit in Figs. 14 and 15 are employed to obtain the frequency response plot of $G_{ro}(s)$ and $Z_o(s)$. The control parameters for MDCS-MPC is set as: $\alpha_1 = 1, \alpha_2 = 0.5, \mu = 11, \lambda = 1,$ and $V_m = 10$ V. Fig. 35 shows the swept results for $G_{ro}(s)$ and $Z_o(s)$. In light of the observation of plots in Fig. 35, it can be concluded that the MDCS-MPC presents smaller output impedance compared to the predictive current and feedback only approaches across the frequency range under test. As shown in Fig. 27, the MDCS-MPC has lower voltage overshoot under step change on load and output reference, compared to feedback-only or VDPC.The MDCS-MPC also features a transfer function $G_{ro}(s)$, which always stays below 0 dB. The MDCS-MPS is also employed to control the DAB with TPS modulation [28].

H. Comparison of Output Voltage Control Methods

The aforementioned control methods are compared in this section. The control parameters are summarized in Table III. These parameters are chosen such that the open loop of each method achieves a 1.2-kHz crossover frequency with 45° phase margin. Based on the theoretical transfer function or the bode plot, these PI parameters can be calculated.

Table IV compares these control methods in terms of implementation complexity, dynamic performance, robustness against parameter variation, and implementation cost. The implementation cost includes costs of voltage/current sensors and microprocessor computational power for the method to be functioning. The required microprocessor computational power is related to the control method complexity. The high-cost methods are those with high implementation complexity and three sensors. The low-cost methods are those with low complexity and one sensor. The FFCC and MDCS-MPC have a higher implementation cost compared to other control methods. The detailed remarks are given as follows. Note that these remarks are only based on theoretical analysis and simulations, and are not validated using experimental results. Practical performance of these control methods can be different from that listed in Table IV.

1) The feedback-only control approach shows mediocre dynamic performance, however, it is easy to implement and requires only one transducer.
2) The linearization control can transform the control loop into the linear system and can counterbalance the influence of the terminal voltage and load variation theoretically, however, its performance deteriorates when circuit parameters used in the control are different from the actual circuit parameters. Besides, the linearization is actually not required since the closed-loop bandwidth and output impedance of the feedback-only control almost does not vary with different output voltage or load conditions.
3) The OCFF control can significantly reduce the output impedance and present a perfect load current disturbance rejection capability, however, its performance deteriorates quickly when there are parameter uncertainties. As shown in Fig. 24, when $L = 1.3L_0$, the output impedance of the OCFF control becomes the same as that of the feedback-only control.
4) The VDPC tries to solve the parameter sensitivity problem of the OCFF control by using the PI output to estimate the phase shift. The biggest problem of the VDPC is that the loop gain varies significantly under different load conditions. Under light load conditions, the bandwidth is too narrow and output impedance is too high, leading to a poor performance on voltage tracking and load current disturbance rejection.
5) The DOBC employs an observer to estimate the total disturbances and uncertainties, and corresponding compensation is generated by making use of the estimate. As a result, the DOBC shows much smaller output impedance

compared with feedback-only control. The performance of the DOBC is not sensitive to the parameter variation. Besides, only one transducer is required.

6) The FFCC is essentially a peak current mode control method with feedforward compensation. The DAB with the FFCC has a small output impedance since the changes on the output current or voltage can lead to immediate change at the inductor current. In the presence of the parameter tolerance, the performance of the FFCC degrades less significantly compared to the OCFF control. However, the FFCC is susceptible to noise, especially when the DAB loses ZVS-ON.
7) The predictive current control can also improve the dynamic performance. Under the same control bandwidth, the output impedance of the predictive current control is lower than that of the feedback-only control. This method may not be feasible for high-frequency applications, since ac sampling and computation are required for each switching cycle.
8) MDCS-MPC has similar ability in load disturbance rejection with the OCFF control. In the meantime, the MDCS-MPC provides salient output voltage tracking performance. However, the MDCS-MPC demands relatively heavy computation power, which is a common issue as with other model predictive control. The control parameters such as weighting factors and the number of points calculated in one control cycle have a significant impact on the control performance. Inappropriate control parameters will cause system instability. Compared with the feedback-only control, the parameters are mainly selected based on trial and error or the machine learning approach. This complicates the design.
9) The methods with the lowest and highest computational reported complexity are the feedback-only control and MDCS-MPC, respectively. According to [28], with the Texas Instruments TMS320F2837xD MCU, the computation time of the feedback-only control and MDCS-MPC is 4.2 and 18.6 μs, respectively. The computation times of other methods are between these two values.

IV. Some Practical Control Issues

This section surveys some practical control issues including dead-time effect, phase drift, and dc offset during dynamic transition.

1) Dead Time Effect: During the dead time period of a leg, the power devices turn OFF and the leg voltages (v_a and v_b in Fig. 41) only depend on the current direction. If the dead time is too long, the voltage may change polarity during this period [71]–[75]. Consider a DAB modulated using SPS, during the dead time of the primary-side H-bridge, all the power devices are "OFF" as shown in Fig. 41, v_{ab} may change polarity if the dead time is too long, leading to undesirable voltage spikes, as shown in Fig. 42 [32], [75]. This phenomenon will bring electromagnetic interference [71] and should be avoided by choosing a proper dead time.

The upper limit for the dead time to prevent the voltage spikes can be estimated assuming linear transformer behavior and ZVS-ON transition. For a DAB modulated using the SPS, the maximum dead time for the primary-side device is [76]

$$t_{\text{dead. max}} = \frac{I_{\text{sw}} \cdot L}{V_1 + NV_2} \tag{73}$$

where I_{sw} is the inductor current at the switching instance.

2) Phase Drift: The actual phase shift can be different from the theoretical one given in (1). There are a few reasons for the phase drift. The first reason is the voltage drop on power devices and other components. Consider a DAB transfers positive power using the SPS modulation as shown in Fig. 43(a). When $t < T_h$, $v_{ab} = V_1 - i_L R_{\text{eq}}$, as shown in Fig. 43(b), where R_{eq} is the equivalent resistances of the primary side; while $T_h < t < T_s$, $v_{ab} = -V_1 - i_L R_{\text{eq}}$. These voltage drops cause the equivalent phase of v_{ab} and v'_{cd} shift to the left and right, respectively. In the case of Fig. 43, the given phase shift is $\phi < 0$, but the phase between the fundamental components of v_{ab} and v'_{cd} $\phi_{(1)} > 0$ and the power is transferred from left to right.

The second reason is the dead time. As explained in Fig. 41, during the dead time, the H-bridge output voltage depends on the current direction and its actual phase may vary from the given ϕ [71], [74], [75].

Another important reason for phase drift is the switching delay during the ZVS transition [76]. A large inductor current will shorten the ZVS transition period, and the phase drift is severest when the switching currents on the primary and secondary sides deviate considerably from each other as shown in Fig. 44.

3) DC Magnetic Flux Bias: In practice, a dc magnetic flux bias will arise both in steady state and transient process for a DAB converter. As shown in Fig. 45, the steady-state dc bias is caused by unmatched parameters of the circuit, like small discrepancy of the gate-drive signal, different turn ON/OFF delay and unequal ON-state resistance of the power devices; while the transient dc bias (see Fig. 46) is caused by the temporary volt-second imbalance on the inductor due to the update of the phase-shift ratio. The steady-state dc bias will increase the conduction losses of the transformer and power devices and lead to loss of ZVS, whereas the transient dc bias may saturate magnetic cores of the transformer and inductor, leading to the failure of the converter in the end [77].

The simplest way to suppress the steady-state dc magnetic flux bias is to include "dc-blocking capacitors" in series with the transformer winding, this will, however, increase the system volume and cost, especially in high-voltage high-power applications. This dc bias can also be eliminated by active controlling the inductor current. One of the prerequisites of this control is to accurately measure the steady-state dc bias, the following measurement methods have been proposed.

1) *Digital sampling and averaging*: Sample the inductor current several times each switching cycle and average the sampled values [80].
2) *Magnetic ear*: An auxiliary circuit shares the magnetic path with the DAB transformer core and senses the flux bias using the integrator circuit [81].

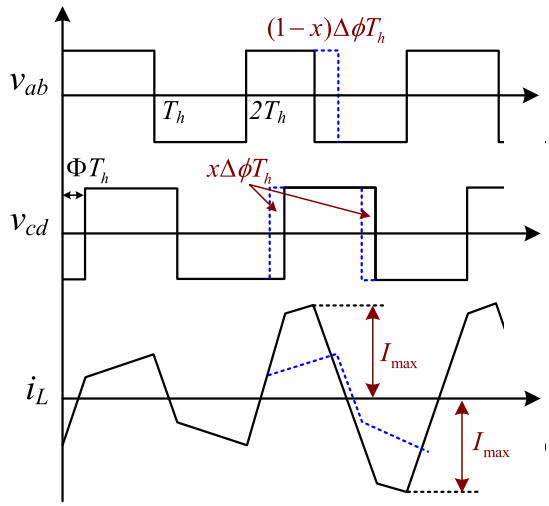

Fig. 47. Typical i_L dc offset suppression method for a DAB when $M < 1$, $x = 1/(1 + M)$ [79].

3) *Analog integration circuit*: Primary- and secondary-side transformer currents are integrated using an analog integration circuit based on operational amplifier (op-amp) [77]. An active reset switch is added to periodically reset the integration circuit to avoid output offset caused by the internal bias current and voltage of the op-amp.

The measured dc bias is then used to regulate the duty cycle of primary- and secondary-side square voltages to eliminate the dc bias. The transfer function from duty cycle to the steady-state bias current as well as the controller design are detailed in [77].

The most common methods to suppress the transient dc offset in the inductor current is to change the phase shift ratio (Φ to $\Phi + \Delta\phi$) by a two-step manner [79], [82]–[84]. Fig. 47 shows a typical example, and during the intermediate step, the falling edge of v_{ab} shrinks $(1 - x)\Delta\phi T_h$, and v_{cd} shifts $x\Delta\phi T_h$, and the resultant i_L has no offset. To eliminate dc offset in both inductor current and transformer magnetizing current, duty cycles of v_{ab} and v_{cd} and their phase shifts have to be manipulated [78]. The two-step methods have been concluded, reviewed, and compared in [85], and this method is extended to DAB converters using the TPS [86].

Another method to suppress transient dc offset is to simply limit the peak inductor current [77]. When the inductor exceeds a preset threshold value, one of the H-bridges will change the output polarity ignoring phase shift command given by the controller. The peak current limit method in [77] is acceptable since the primary purpose of the transient dc offset suppression is to avoid magnetic components saturation. When the magnetic component saturation is avoided, the transient dc bias will be settled down by the parasitic resistance as shown in Fig. 46(b).

V. Conclusion

This work reviews the modeling and control for the DAB dc–dc converter. Three types of modeling techniques, i.e., reduced-order model, generalized average model, and discrete-time model, are comprehensively introduced and critically compared based on simulation results. The model accuracy and complexity of each method are summarized in Table II. The reduced-order model has the best overall performance due to its simplicity and good conformity to the simulation results. The reduced-order model is of first order and inductance does not affect the DAB dynamic performance, similar to that of the traditional dc–dc converter operating in discontinuous mode (DCM). For high-frequency DAB where the ZVS intervals have significant impact on dynamics, the discrete-time model may be a better choice.

Different control methods including feedback control, linearization control, feedforward plus feedback, DOBC, FFCC, model predictive current control, SMC, and MDCS-MPC are reviewed and compared. The closed-loop control-to-output $G_{ro}(s)$ and output impedance $Z_o(s)$ are selected as the metrics of the ability in voltage tracking and the load disturbance rejection performance. Table IV compares the performance of these control methods. Detailed remarks are also provided at the end of Section III. The DOBC shows excellent dynamic performance, better than the feedback-only control. Besides, the DOBC is not sensitive to the parameter variations and only requires one transducer. MDCS-MPC, FFCC, and more predictive current control also show excellent dynamic performance. However, these methods require three transducers. Besides, the control parameters of MDCS-MPC should be chosen based on trial-and-error or the machine learning. The FFCC can be affected by the switching noise (similar to peak current mode control). The predictive current control is not suitable for high-frequency applications and is sensitive to parameter variation.

Practical control issues including dead-time effect, phase drift, and dc magnetic flux bias are also reviewed. The causes of these issues are comprehensively explained. The dead-time effect can be avoided by choosing proper dead time. Phase drift can be caused by the voltage drop on components, dead time, and switching delay during the ZVS transitions. Integral term should always be included in the control loop to compensate the phase drift. In terms of the dc magnetic flux bias, the steady-state dc bias can be suppressed using dc-blocking capacitors or active control of the inductor current. The transient dc bias can be suppressed by changing the phase shift ratio in two steps or by simply limiting the peak current during the transient period.

With the development of advanced modulation methods and wide adoption of WBG devices, there are several new challenges in modeling and control DAB converters. Firs, there is a research gap on how to apply these control methods to DAB in conjunction with advanced modulations. The existing control methods are mostly for DAB with SPS. However, more and more research proposes advanced modulations for DABs, such as DPS, TPS, or frequency modulation, where either the duty cycles or frequencies of the square voltages are regulated. These advanced modulation methods can effectively suppress the circulating current and expand ZVS-ON region. To apply these advanced modulation methods in practice, it is necessary to build the models and coordinate the existing control methods with these modulations.

Second, for DAB with WBG devices, the sampling and control delays as well as the ZVS transition can occupy a considerable percentage of the overall microprocessor calculation period [35],

[36]. Besides, the high dv/dt introduced by WBG devices can lead to inductor current oscillations and control instability [87], and the ZVS of GaN devices can be affected by transformer parasitic capacitance [88]. To face these challenges, more detailed circuit model is required for these applications.

Third, only resistive load is considered in evaluating the control methods, however, there are many other types of loads, such as constant power load (CPL) and pulsed power load (PPL). A typical CPL is the tightly regulated power electronics load, which exhibits negative incremental impedance characteristics [89]. The CPLs decrease the system damping. On the other hand, PPLs draw a large amount of power in a very short period, resulting in voltage sags. PPL is common in onboard microgrids like more electric aircrafts, electric ships, or fast EV charging stations [89]. These two types of loads can push the system more easily beyond its safe operating margins compared to resistive loads [68], [89]. It is thus necessary to evaluate the DAB control methods under CPLs and PPLs to verify their performance in the most challenging scenarios. Other advanced control methods such as backstepping [89], [90], passivity-based controllers [91], and intelligent control [92] can also be applied to control DAB with CPLs and PPLs.

REFERENCES

[1] T. Dragičević, X. Lu, J. C. Vasquez, and J. M. Guerrero, "DC microgrids—Part I: A review of control strategies and stabilization techniques," *IEEE Trans. Power Electron.*, vol. 31, no. 7, pp. 4876–4891, Jul. 2016.

[2] D. Boroyevich, I. Cvetković, D. Dong, R. Burgos, F. Wang, and F. Lee, "Future electronic power distribution systems a contemplative view," in *Proc. 12th Int. Conf. Optim. Elect. Electron. Equip.*, May 2010, pp. 1369–1380.

[3] Y. Gu, "Distributed peer-to-peer control for renewable power generation DC microgrid," Ph.D. dissertation, College Elect. Eng., Zhejiang Univ., Hangzhou, China, Jul. 2015. [Online]. Available: https://www.cnki.net/

[4] B. Zhao, Q. Song, W. Liu, and Y. Sun, "Overview of dual-active-bridge isolated bidirectional DC-DC converter for high-frequency-link power-conversion system," *IEEE Trans. Power Electron.*, vol. 29, no. 8, pp. 4091–4106, Aug. 2014.

[5] R. W. D. Doncker, D. M. Divan, and M. H. Kheraluwala, "A three-phase soft-switched high power density DC/DC converter for high power applications," in *Proc. IEEE Ind. Appl. Soc. Annu. Meeting*, Oct. 1988, vol. 1, pp. 796–805.

[6] R. W. A. A. D. Doncker, D. M. Divan, and M. H. Kheraluwala, "A three-phase soft-switched high-power-density DC/DC converter for high-power applications," *IEEE Trans. Ind. Appl.*, vol. 27, no. 1, pp. 63–73, Jan. 1991.

[7] S. Shao, H. Chen, X. Wu, J. Zhang, and K. Sheng, "Circulating current and ZVS-on of a dual active bridge DC-DC converter: A review," *IEEE Access*, vol. 7, pp. 50 561–50 572, 2019.

[8] A. Q. Huang, M. L. Crow, G. T. Heydt, J. P. Zheng, and S. J. Dale, "The future renewable electric energy delivery and management (FREEDM) system: The energy internet," *Proc. IEEE*, vol. 99, no. 1, pp. 133–148, Jan. 2011.

[9] B. Zhao, Q. Song, J. Li, and W. Liu, "A modular multilevel DC-link front-to-front DC solid-state transformer based on high-frequency dual active phase shift for HVDC grid integration," *IEEE Trans. Ind. Electron.*, vol. 64, no. 11, pp. 8919–8927, Nov. 2017.

[10] S. Shao, M. Jiang, J. Zhang, and X. Wu, "A capacitor voltage balancing method for a modular multilevel DC transformer for DC distribution system," *IEEE Trans. Power Electron.*, vol. 33, no. 4, pp. 3002–3011, Apr. 2018.

[11] D. Dujic *et al.*, "Power electronic traction transformer-low voltage prototype," *IEEE Trans. Power Electron.*, vol. 28, no. 12, pp. 5522–5534, Dec. 2013.

[12] C. Zhao *et al.*, "Power electronic traction transformer-medium voltage prototype," *IEEE Trans. Ind. Electron.*, vol. 61, no. 7, pp. 3257–3268, Jul. 2014.

[13] L. Xue, Z. Shen, D. Boroyevich, P. Mattavelli, and D. Diaz, "Dual active bridge-based battery charger for plug-in hybrid electric vehicle with charging current containing low frequency ripple," *IEEE Trans. Power Electron.*, vol. 30, no. 12, pp. 7299–7307, Dec. 2015.

[14] J. Lu *et al.*, "A modular-designed three-phase high-efficiency high-power-density EV battery charger using dual/triple-phase-shift control," *IEEE Trans. Power Electron.*, vol. 33, no. 9, pp. 8091–8100, Sep. 2018.

[15] Z. Zhang, J. Huang, and Y. Xiao, "GaN-based 1-MHz partial parallel dual active bridge converter with integrated magnetics," *IEEE Trans. Ind. Electron.*, vol. 68, no. 8, pp. 6729–6738, Aug. 2021.

[16] W. Xu, R. y. Yu, Z. Guo, and A. Q. Huang, "Design of 1500V/200kW 99.6 efficiency dual active bridge converters based on 1700V SiC power MOSFET module," in *Proc. IEEE Energy Convers. Congr. Expo.*, 2020, pp. 6000–6007.

[17] W. Xu *et al.*, "Hardware design and demonstration of a 100kW, 99 half bridge converter based on 1700v SiC power MOSFET," in *Proc. IEEE Appl. Power Electron. Conf. Expo.*, 2020, pp. 1367–1373.

[18] S. Inoue and H. Akagi, "A bidirectional DC-DC converter for an energy storage system with galvanic isolation," *IEEE Trans. Power Electron.*, vol. 22, no. 6, pp. 2299–2306, Nov. 2007.

[19] C. Gammeter, F. Krismer, and J. W. Kolar, "Comprehensive conceptualization, design, and experimental verification of a weight-optimized all-SiC 2 kV/700 V DAB for an airborne wind turbine," *IEEE Trans. Emerg. Sel. Topics Power Electron.*, vol. 4, no. 2, pp. 638–656, Jun. 2016.

[20] Y. W. Cho, W. J. Cha, J. M. Kwon, and B. H. Kwon, "High-efficiency bidirectional DAB inverter using a novel hybrid modulation for stand-alone power generating system with low input voltage," *IEEE Trans. Power Electron.*, vol. 31, no. 6, pp. 4138–4147, Jun. 2016.

[21] H. Y. Kanaan, M. Caron, and K. Al-Haddad, "Design and implementation of a two-stage grid-connected high efficiency power load emulator," *IEEE Trans. Power Electron.*, vol. 29, no. 8, pp. 3997–4006, Aug. 2014.

[22] N. Hou and Y. W. Li, "Overview and comparison of modulation and control strategies for a nonresonant single-phase dual-active-bridge DC-DC converter," *IEEE Trans. Power Electron.*, vol. 35, no. 3, pp. 3148–3172, Mar. 2020.

[23] A. S. Babokany, M. Jabbari, G. Shahgholian, and M. Mahdavian, "A review of bidirectional dual active bridge converter," in *Proc. 9th Int. Conf. Elect. Eng./Electron., Comput., Telecommun. Inf. Technol.*, May 2012, pp. 1–4.

[24] R. W. Erickson and D. Maksimovic, *Fundamentals of Power Electronics*. New York, NY, USA: Springer, 2007.

[25] A. R. Alonso, J. Sebastian, D. G. Lamar, M. M. Hernando, and A. Vazquez, "An overall study of a dual active bridge for bidirectional DC/DC conversion," in *Proc. IEEE Energy Convers. Congr. Expo.*, Sep. 2010, pp. 1129–1135.

[26] H. Bai, C. Mi, C. Wang, and S. Gargies, "The dynamic model and hybrid phase-shift control of a dual-active-bridge converter," in *Proc. 34th Annu. Conf. IEEE Ind. Electron.*, Nov. 2008, pp. 2840–2845.

[27] H. Bai, Z. Nie, and C. C. Mi, "Experimental comparison of traditional phase-shift, dual-phase-shift, and model-based control of isolated bidirectional DC-DC converters," *IEEE Trans. Power Electron.*, vol. 25, no. 6, pp. 1444–1449, Jun. 2010.

[28] L. Chen, L. Lin, S. Shao, F. Gao, Z. Wang, P. W. Wheeler, and T. Dragičević, "Moving discretized control set model-predictive control for dual-active bridge with the triple-phase shift," *IEEE Trans. Power Electron.*, vol. 35, no. 8, pp. 8624–8637, Aug. 2020.

[29] K. Zhang, Z. Shan, and J. Jatskevich, "Large- and small-signal average-value modeling of dual-active-bridge DC-DC converter considering power losses," *IEEE Trans. Power Electron.*, vol. 32, no. 3, pp. 1964–1974, Mar. 2017.

[30] V. A. Caliskan, O. C. Verghese, and A. M. Stankovic, "Multifrequency averaging of DC/DC converters," *IEEE Trans. Power Electron.*, vol. 14, no. 1, pp. 124–133, Jan. 1999.

[31] H. Qin and J. W. Kimball, "Generalized average modeling of dual active bridge DC-DC converter," *IEEE Trans. Power Electron.*, vol. 27, no. 4, pp. 2078–2084, Apr. 2012.

[32] D. Segaran, D. G. Holmes, and B. P. McGrath, "Enhanced load step response for a bidirectional DC-DC converter," *IEEE Trans. Power Electron.*, vol. 28, no. 1, pp. 371–379, Jan. 2013.

[33] C. Zhao, S. D. Round, and J. W. Kolar, "Full-order averaging modelling of zero-voltage-switching phase-shift bidirectional DC-DC converters," *IET Power Electron.*, vol. 3, no. 3, pp. 400–410, May 2010.

[34] F. Krismer and J. W. Kolar, "Accurate small-signal model for the digital control of an automotive bidirectional dual active bridge," *IEEE Trans. Power Electron.*, vol. 24, no. 12, pp. 2756–2768, Dec. 2009.

[35] D. Costinett, R. Zane, and D. Maksimović, "Discrete-time small-signal modeling of a 1 MHz efficiency-optimized dual active bridge converter with varying load," in *Proc. IEEE 13th Workshop Control Model. Power Electron.*, Jun. 2012, pp. 1–7.

[36] D. Costinett, "Reduced order discrete time modeling of ZVS transition dynamics in the dual active bridge converter," in *Proc. IEEE Appl. Power Electron. Conf. Expo.*, Mar. 2015, pp. 365–370.

[37] L. Shi, W. Lei, Z. Li, J. Huang, Y. Cui, and Y. Wang, "Bilinear discrete-time modeling and stability analysis of the digitally controlled dual active bridge converter," *IEEE Trans. Power Electron.*, vol. 32, no. 11, pp. 8787–8799, Nov. 2017.

[38] D. Maksimovic and R. Zane, "Small-signal discrete-time modeling of digitally controlled PWM converters," *IEEE Trans. Power Electron.*, vol. 22, no. 6, pp. 2552–2556, Nov. 2007.

[39] S. Shao, M. Jiang, W. Ye, Y. Li, J. Zhang, and K. Sheng, "Optimal phase-shift control to minimize reactive power for a dual active bridge DC-DC converter," *IEEE Trans. Power Electron.*, vol. 34, no. 10, pp. 10193–10205, Oct. 2019.

[40] J. Huang, Y. Wang, Z. Li, and W. Lei, "Unified triple-phase-shift control to minimize current stress and achieve full soft-switching of isolated bidirectional DC-DC converter," *IEEE Trans. Ind. Electron.*, vol. 63, no. 7, pp. 4169–4179, Jul. 2016.

[41] G. Xu, D. Sha, J. Zhang, and X. Liao, "Unified boundary trapezoidal modulation control utilizing fixed duty cycle compensation and magnetizing current design for dual active bridge DC-DC converter," *IEEE Trans. Power Electron.*, vol. 32, no. 3, pp. 2243–2252, Mar. 2017.

[42] G. G. Oggier, G. O. GarcÍa, and A. R. Oliva, "Switching control strategy to minimize dual active bridge converter losses," *IEEE Trans. Power Electron.*, vol. 24, no. 7, pp. 1826–1838, Jul. 2009.

[43] M. N. Kheraluwala, R. W. Gascoigne, D. M. Divan, and E. D. Baumann, "Performance characterization of a high-power dual active bridge DC-to-DC converter," *IEEE Trans. Ind. Appl.*, vol. 28, no. 6, pp. 1294–1301, Nov. 1992.

[44] H. Qin and J. W. Kimball, "Closed-loop control of DC-DC dual-active-bridge converters driving single-phase inverters," *IEEE Trans. Power Electron.*, vol. 29, no. 2, pp. 1006–1017, Feb. 2014.

[45] A. Tong, L. Hang, H. S. Chung, G. Li, K. Wang, and Y. He, "Using sampled-data modeling method to derive equivalent circuit and linearized control method for dual-active-bridge converter," *IEEE Trans. Emerg. Sel. Topics Power Electron.*, vol. 9, no. 2, pp. 1361–1374, Apr. 2021.

[46] F. An, W. Song, K. Yang, N. Hou, and J. Ma, "Improved dynamic performance of dual active bridge DC-DC converters using MPC scheme," *IET Power Electron.*, vol. 11, no. 11, pp. 1756–1765, 2018.

[47] W. Zhao, X. Zhang, S. Gao, and M. Ma, "Improved model-based phase-shift control for fast dynamic response of dual active bridge DC/DC converters," *IEEE Trans. Emerg. Sel. Topics Power Electron.*, vol. 9, no. 1, pp. 223–231, Feb. 2021.

[48] W. Song, N. Hou, and M. Wu, "Virtual direct power control scheme of dual active bridge DC-DC converters for fast dynamic response," *IEEE Trans. Power Electron.*, vol. 33, no. 2, pp. 1750–1759, Feb. 2018.

[49] W. Chen, J. Yang, L. Guo, and S. Li, "Disturbance-observer-based control and related methods—An overview," *IEEE Trans. Ind. Electron.*, vol. 63, no. 2, pp. 1083–1095, Feb. 2016.

[50] M. Ali, M. Yaqoob, L. Cao, and K. H. Loo, "Disturbance-observer-based DC-bus voltage control for ripple mitigation and improved dynamic response in two-stage single-phase inverter system," *IEEE Trans. Ind. Electron.*, vol. 66, no. 9, pp. 6836–6845, Sep. 2019.

[51] F. Xiong, J. Wu, Z. Liu, and L. Hao, "Current sensorless control for dual active bridge DC-DC converter with estimated load-current feedforward," *IEEE Trans. Power Electron.*, vol. 33, no. 4, pp. 3552–3566, Apr. 2018.

[52] Y. Wu, M. Mahmud, Y. Zhao, and H. A. Mantooth, "Uncertainty and disturbance estimator based robust tracking control for dual-active-bridge converters," *IEEE Trans. Transport. Electrific.*, vol. 6, no. 4, pp. 1791–1800, Dec. 2020.

[53] Z. Shan, J. Jatskevich, H. H. Iu, and T. Fernando, "Simplified load-feedforward control design for dual-active-bridge converters with current-mode modulation," *IEEE Trans. Emerg. Sel. Topics Power Electron.*, vol. 6, no. 4, pp. 2073–2085, Dec. 2018.

[54] S. Tan, P. Lin, C. Hu, L. Chen, and D. Xu, "Interleaved flyback micro-inverter with SiC MOSFET," in *Proc. Int. Power Electron. Appl. Conf. Expo.*, Nov. 2014, pp. 285–290.

[55] L. Dixon, "Average current mode control of switching power supplies," Texas Instruments, 1990. [Online]. Available: https://www.ti.com/seclit/ml/slup091/slup091.pdf

[56] S. Dutta, S. Hazra, and S. Bhattacharya, "A digital predictive current-mode controller for a single-phase high-frequency transformer-isolated dual-active bridge DC-to-DC converter," *IEEE Trans. Ind. Electron.*, vol. 63, no. 9, pp. 5943–5952, Sep. 2016.

[57] S. Dutta, S. Bhattacharya, and M. Chandorkar, "A novel predictive phase shift controller for bidirectional isolated DC to DC converter for high power applications," in *Proc. IEEE Energy Convers. Congr. Expo.*, Sep. 2012, pp. 418–423.

[58] L. Zhu, A. R. Taylor, G. Liu, and K. Bai, "A multiple-phase-shift control for a SiC-based EV charger to optimize the light-load efficiency, current stress, and power quality," *IEEE Trans. Emerg. Sel. Topics Power Electron.*, vol. 6, no. 4, pp. 2262–2272, Dec. 2018.

[59] S.-C. Tan, Y.-M. Lai, and C.-K. Tse, *Sliding Mode Control of Switching Power Converters: Techniques and Implementation*. Boca Raton, FL, USA: CRC Press, 2011.

[60] A. R. Brown and R. D. Middlebrook, "Sampled-data modeling of switching regulators," in *Proc. IEEE Power Electron. Specialists Conf.*, Jun. 1981, pp. 349–369.

[61] D. C. Hamill, J. H. B. Deane, and D. J. Jefferies, "Modeling of chaotic DC-DC converters by iterated nonlinear mappings," *IEEE Trans. Power Electron.*, vol. 7, no. 1, pp. 25–36, Jan. 1992.

[62] V. Utkin, J. Guldner, and J. Shi, *Sliding Mode Control in Electro-Mechanical Systems*. Boca Raton, FL, USA: CRC Press, 2009.

[63] Y. Jeung and D. Lee, "Voltage and current regulations of bidirectional isolated dual-active-bridge DC-DC converters based on a double-integral sliding mode control," *IEEE Trans. Power Electron.*, vol. 34, no. 7, pp. 6937–6946, Jul. 2019.

[64] K. Li, Y. Yang, S. Tan, and R. S. Hui, "Sliding-mode-based direct power control of dual-active-bridge DC-DC converters," in *Proc. IEEE Appl. Power Electron. Conf. Expo.*, Mar. 2019, pp. 188–192.

[65] P. Mattavelli, L. Rossetto, G. Spiazzi, and P. Tenti, "General-purpose sliding-mode controller for DC/DC converter applications," in *Proc. IEEE Power Electron. Spec. Conf.*, Jun. 1993, pp. 609–615.

[66] V. M. Nguyen and C. Q. Lee, "Indirect implementations of sliding-mode control law in buck-type converters," in *Proc. Appl. Power Electron. Conf.*, Mar. 1996, vol. 1, pp. 111–115.

[67] S. Tan, Y. M. Lai, and C. K. Tse, "Indirect sliding mode control of power converters via double integral sliding surface," *IEEE Trans. Power Electron.*, vol. 23, no. 2, pp. 600–611, Mar. 2008.

[68] L. Chen, S. Shao, Q. Xiao, L. Tarisciotti, T. Dragicevic, and P. Wheeler, "Model-predictive-control for dual-active-bridge converters supplying pulsed power loads in naval DC microgrids," *IEEE Trans. Power Electron.*, vol. 35, pp. 1957–1966, Feb. 2020.

[69] L. Chen, L. Tarisciotti, A. Costabeber, P. Wheeler, and P. Zanchetta, "Model predictive control for isolated DC/DC power converters with transformer peak current shaving," in *Proc. IEEE Energy Convers. Congr. Expo.*, Sep. 2018, pp. 5954–5960.

[70] L. Chen, F. Gao, K. Shen, Z. Wang, L. Tarisciotti, P. Wheeler, and T. Dragičević, "Predictive control based DC microgrid stabilization with the dual active bridge converter," *IEEE Trans. Ind. Electron.*, vol. 67, no. 10, pp. 8944–8956, Oct. 2020.

[71] H. Bai, C. C. Mi, and S. Gargies, "The short-time-scale transient processes in high-voltage and high-power isolated bidirectional DC-DC converters," *IEEE Trans. Power Electron.*, vol. 23, no. 6, pp. 2648–2656, Nov. 2008.

[72] J. Li, Z. Chen, Z. Shen, P. Mattavelli, J. Liu, and D. Boroyevich, "An adaptive dead-time control scheme for high-switching-frequency dual-active-bridge converter," in *Proc. 27th Annu. IEEE Appl. Power Electron. Conf. Expo.*, Feb. 2012, pp. 1355–1361.

[73] D. Costinett, R. Zane, and D. Maksimovic, "Automatic voltage and dead time control for efficiency optimization in a dual active bridge converter," in *Proc. 27th Annu. IEEE Appl. Power Electron. Conf. Expo.*, Feb. 2012, pp. 1104–1111.

[74] B. Zhao, Q. Song, W. Liu, and Y. Sun, "Dead-time effect of the high-frequency isolated bidirectional full-bridge DC-DC converter: Comprehensive theoretical analysis and experimental verification," *IEEE Trans. Power Electron.*, vol. 29, no. 4, pp. 1667–1680, Apr. 2014.

[75] J. Riedel, D. G. Holmes, B. P. McGrath, and C. Teixeira, "ZVS soft switching boundaries for dual active bridge DC-DC converters using frequency domain analysis," *IEEE Trans. Power Electron.*, vol. 32, no. 4, pp. 3166–3179, Apr. 2017.

[76] J. Hiltunen, V. Väisänen, R. Juntunen, and P. Silventoinen, "Variable-frequency phase shift modulation of a dual active bridge converter," *IEEE Trans. Power Electron.*, vol. 30, no. 12, pp. 7138–7148, Dec. 2015.

[77] B. Zhang, S. Shao, L. Chen, X. Wu, and J. Zhang, "Steady state and transient DC magnetic flux bias suppression methods for a dual active bridge converter," *IEEE Trans. Emerg. Sel. Topics Power Electron.*, vol. 9, no. 1, pp. 744–753, Feb. 2021.
[78] K. Takagi and H. Fujita, "Dynamic control and performance of a dual-active-bridge DC-DC converter," *IEEE Trans. Power Electron.*, vol. 33, no. 9, pp. 7858–7866, Sep. 2018.
[79] X. Li and Y. F. Li, "An optimized phase-shift modulation for fast transient response in a dual-active-bridge converter," *IEEE Trans. Power Electron.*, vol. 29, no. 6, pp. 2661–2665, Jun. 2014.
[80] S. Dutta and S. Bhattacharya, "A method to measure the DC bias in high frequency isolation transformer of the dual active bridge DC to DC converter and its removal using current injection and PWM switching," in *Proc. IEEE Energy Convers. Congr. Expo.*, Sep. 2014, pp. 1134–1139.
[81] G. Ortiz, L. Fässler, J. W. Kolar, and O. Apeldoorn, "Flux balancing of isolation transformers and application of "the magnetic ear" for closed-loop volt-second compensation," *IEEE Trans. Power Electron.*, vol. 29, no. 8, pp. 4078–4090, Aug. 2014.
[82] S. P. Engel, N. Soltau, H. Stagge, and R. W. D. Doncker, "Dynamic and balanced control of three-phase high-power dual-active bridge DC-DC converters in DC-grid applications," *IEEE Trans. Power Electron.*, vol. 28, no. 4, pp. 1880–1889, Apr. 2013.
[83] B. Zhao, Q. Song, W. Liu, and Y. Zhao, "Transient DC bias and current impact effects of high-frequency-isolated bidirectional DC-DC converter in practice," *IEEE Trans. Power Electron.*, vol. 31, no. 4, pp. 3203–3216, Apr. 2016.
[84] S. T. Lin, X. Li, C. Sun, and Y. Tang, "Fast transient control for power adjustment in a dual-active-bridge converter," *Electron. Lett.*, vol. 53, no. 16, pp. 1130–1132, 2017.
[85] Y. Tang, X. Li, S. Zhou, C. Sun, and G. Chen, "Comprehensive study of fast load modulation with volt-second balance in a dual-active-bridge converter," *IET Power Electron.*, vol. 12, no. 6, pp. 1357–1367, 2019.
[86] C. Sun, X. Li, and S. Zhou, "Transient current control for a step load change in a dual-active-bridge converter," *Electron. Lett.*, vol. 54, no. 22, pp. 1290–1292, 2018.
[87] B. Cui, H. Shi, Q. Sun, X. Tang, L. Hong, and B. Zhao, "A novel analysis, design, and optimal methodology of high-frequency oscillation for dual active bridge converters with WBG switching devices and nanocrystalline transformer cores," *IEEE Trans. Power Electron.*, vol. 36, no. 7, pp. 7665–7678, Jul. 2021.
[88] Y. Xiao, Z. Zhang, M. A. E. Andersen, and K. Sun, "Impact on ZVS operation by splitting inductance to both sides of transformer for 1-MHz GaN based DAB converter," *IEEE Trans. Power Electron.*, vol. 35, no. 11, pp. 11988–12002, Nov. 2020.
[89] Q. Xu, N. Vafamand, L. Chen, T. Dragičević, L. Xie, and F. Blaabjerg, "Review on advanced control technologies for bidirectional DC/DC converters in DC microgrids," *IEEE Trans. Emerg. Sel. Topics Power Electron.*, vol. 9, no. 2, pp. 1205–1221, Apr. 2021.
[90] S. Yousefizadeh, J. D. Bendtsen, N. Vafamand, M. H. Khooban, F. Blaabjerg, and T. Dragičević, "Tracking control for a DC microgrid feeding uncertain loads in more electric aircraft: Adaptive backstepping approach," *IEEE Trans. Ind. Electron.*, vol. 66, no. 7, pp. 5644–5652, Jul. 2019.
[91] J. Zeng, Z. Zhang, and W. Qiao, "An interconnection and damping assignment passivity-based controller for a DC-DC boost converter with a constant power load," *IEEE Trans. Ind. Appl.*, vol. 50, no. 4, pp. 2314–2322, Jul./Aug. 2014.
[92] N. Chettibi, A. Mellit, G. Sulligoi, and A. Massi Pavan, "Adaptive neural network-based control of a hybrid AC/DC microgrid," *IEEE Trans. Smart Grid*, vol. 9, no. 3, pp. 1667–1679, May 2018.

Shuai Shao (Member, IEEE) received the B.S. degree from Zhejiang University, Hangzhou, China, in 2010, and the Ph.D. degree in electrical and electronic engineering from the University of Nottingham, Nottingham, U.K., in 2015.

In 2015, he joined the College of Electrical Engineering, Zhejiang University, as a Lecturer, and was promoted as an Associate Professor in January 2020. His research interests include solid-state transformers, bidirectional dc–dc converters, and fault detection in power converters. He has authored and co-authored more than 40 peer-reviewed journal and conference papers.

Dr. Shao served as a Guest Associate Editor for the IEEE JOURNAL OF EMERGING AND SELECTED TOPICS IN POWER ELECTRONICS and *CES Transactions on Electrical Machines and Systems*.

Linglin Chen received the M.Sc. degree in electrical engineering from Zhejiang University, Hangzhou, China, in 2016 and the Ph.D. degree in electrical and electronics engineering from the University of Nottingham, Nottingham, U.K., in 2020.

From 2018 to 2019, he was a Visiting Scholar with the Department of Energy Technology, Aalborg University, Aalborg, Denmark. From 2019 to 2020, he was a Visiting Scholar with the Key Laboratory of Control of Power Transmission and Transformation, Shanghai Jiao Tong University, Shanghai, China. He joined Digital power Huawei Techonologies, Shenzhen, China, in 2020, and he is currently with Hisillicon of the same company. His interests includes SiC&GaN device and gate driver, PV optimizer and string inverter, telecom&server rectifier, traction inverter etc.

Zhenyu Shan (Member, IEEE) received the B.Eng. and M.Eng. degrees in control engineering from Beijing Jiaotong University, Beijing, China, in 2007 and 2009, respectively, and the Ph.D. degree in electrical engineering from Hong Kong Polytechnic University, Hong Kong, in 2013.

He was a Visiting Student with the University of Illinois at Urbana-Champaign, Champaign, IL, USA, from March to June 2013. He was a Postdoctoral Research Fellow with the University of British Columbia, Vancouver, BC, Canada, from November 2013 to June 2016. He is currently an Assistant Professor and Associate Head with the Department of Electrical Engineering, Beihang University, Beijing. His research interests include modeling and nonlinear control of power electronic circuits.

Dr. Shan is a Professional Committee Member of China Power Supply Society and serves as a Reviewer for various IEEE transactions and other international journals on electrical and electronic engineering. He was selected in Beijing Sea Poly Overseas Young Talent Program with North China University of Technology, Beijing, from 2017 to 2019.

Fei Gao (Member, IEEE) received the Ph.D. degree in electrical engineering from Power Electronics, Machines, and Control Research Group, University of Nottingham, Nottingham, U.K., in 2016.

From March 2010 to September 2012, he has with Jiangsu Electric Power Research Institute, Nanjing, State Grid Corporation of China. From 2016 to 2019, he has been with the Department of Engineering Science, University of Oxford, Oxford, U.K., as a Postdoctoral Researcher. Since July 2019, he has been with Shanghai Jiao Tong University, Shanghai, China, as an Associate Professor. His current research interests include modeling, control, power management, and stability of microgrids and more electric transportation systems.

Dr. Gao was the recipient of the European Union Clean Sky Best Ph.D. Award in 2017 and IET Control and Automation Runner Up Ph.D. Award in 2018.

Hui Chen was born in Zhejiang, China, in 1988. She received the B.S. and Ph.D. degrees in electrical engineering from Zhejiang University, Hangzhou, China, in 2010 and 2015, respectively.

She is currently working as a Lecturer with Zhejiang University City College, Hangzhou. Her current research interests include high-efficiency dc–dc converters and topology research.

Deshang Sha (Senior Member, IEEE) received the B.S. degree from the Luoyang Institute of Technology, Luoyang, China, in 1998, the M.S. degree from the Nanjing University of Aeronautics and Astronautics, Nanjing, China, in 2001, and the Ph.D. degree from the Institute of Electrical Engineering, Chinese Academy of Sciences, Beijing, China, in 2005, all in electrical engineering.

Since 2008, he has been with the School of Automation, Beijing Institute of Technology, Beijing, where he is currently a tenured Associate Professor. From 2012 to 2013, he was a Visiting Scholar with Future Energy Electronics Center, Virginia Polytechnic Institute and State University, Blacksburg, VA, USA. He has authored more than 100 papers and three books. His current research interests include the modeling and control of power converters, and high-efficiency power conversion.

Tomislav Dragičević (Senior Member, IEEE) received the M.Sc. and the industrial Ph.D. degrees in electrical engineering from the Faculty of Electrical Engineering, University of Zagreb, Zagreb, Croatia, in 2009 and 2013, respectively.

From 2013 to 2016, he was a Postdoctoral Researcher with Aalborg University, Aalborg, Denmark, where he was an Associate Professor from 2016 to 2020. He is currently a Professor with the Technical University of Denmark, Kongens Lyngby, Denmark. He made a Guest Professor stay with Nottingham University, Nottingham, U.K., during spring/summer of 2018. His research interests include application of advanced control, optimization and artificial intelligence inspired techniques to provide innovative and effective solutions to emerging challenges in design, control, and diagnostics of power electronics intensive electrical distributions systems and microgrids. He has authored and co-authored more than 330 technical publications (more than 150 of them are published in international journals, mostly in IEEE), ten book chapters, and a book in this field, as well as filed for several patents.

Dr. Dragičević serves as an Associate Editor for the IEEE TRANSACTIONS ON INDUSTRIAL ELECTRONICS, IEEE TRANSACTIONS ON POWER ELECTRONICS, IEEE EMERGING AND SELECTED TOPICS IN POWER ELECTRONICS, and *IEEE Industrial Electronics Magazine*. He was the recipient of the Končar prize for the best industrial Ph.D. thesis in Croatia, a Robert Mayer Energy Conservation award, and an Alexander von Humboldt fellowship for experienced researchers.